Catalysis Science & Technology

Surface Structure Sensitivity of Hydrodeoxygenation of Biomass-derived Organic Acids over Palladium Catalysts: A Microkinetic Modeling Approach

Journal:	*Catalysis Science & Technology*
Manuscript ID	CY-ART-06-2021-001029.R1
Article Type:	Paper
Date Submitted by the Author:	19-Jul-2021

Complete List of Authors:	Kundu, Subrata; University of South Carolina System, Rajadurai, Vijay Solomon; Bharathidasan University, School of Chemistry Yang, Wenqiang; University of South Carolina, Chemical Engineering Walker, Eric; University at Buffalo - The State University of New York, Institute for Computational and Data Sciences; University at Buffalo - The State University of New York, Chemical and Biological Engineering Mamun, Osman; University of South Carolina, Chemical Engineering Bond, Jesse; Syracuse University, Biomedical and Chemical Engineering Heyden, Andreas; University of South Carolina, Chemical Engineering

Surface Structure Sensitivity of Hydrodeoxygenation of Biomass-derived Organic Acids over Palladium Catalysts: A Microkinetic Modeling Approach

Subrata Kumar Kundu,[a] Rajadurai Vijay Solomon,[a] Wenqiang Yang,[a] Eric Walker,[a,b,c] Osman Mamun,[a] Jesse Q. Bond[d] and Andreas Heyden[a,*]

[a]Department of Chemical Engineering, University of South Carolina, 301 South Main Street, Columbia, SC 29208, USA.

[b]Institute for Computational and Data Sciences, University at Buffalo, The State University of New York, Buffalo, New York 14260, USA

[c]Department of Chemical and Biological Engineering, University at Buffalo, The State University of New York, Buffalo, New York 14260, USA

[d]Department of Biomedical and Chemical Engineering, Syracuse University, 329 Link Hall, Syracuse, NY 13244, USA.

† Electronic supplementary information (ESI) available: Effects of solvents, i.e., water and 1,4-dioxane, on reaction free energies and activation energies in eV of all the elementary reaction steps in the HDO of propanoic acid over Pd(100) and Pd(111) at a temperature of 473 K, a propionic acid gas phase partial pressure of 1 bar, a CO gas phase partial pressure of 1×10^{-5} bar, and a hydrogen partial pressure of 0.01 bar using ±10% of the default COSMO palladium cavity radius (Table S1), CO and H lateral interaction coefficients, a_{CO} and a_H, of surface intermediates on Pd(100) and Pd(111) at a temperature of 473 K (Table S2), TOFs (s^{-1}) of various elementary steps on Pd(100) and Pd(111) in water with +10% increased palladium COSMO cavity radius at a temperature of 473 K, a propionic acid gas phase partial pressure of 1 bar, a CO gas phase partial pressure of 1×10^{-5} bar, and a hydrogen partial pressure of 0.01 bar (Fig. S1), TOFs (s^{-1}) of various elementary steps on Pd(100) and Pd(111) in water with –10% decreased palladium COSMO cavity radius at a temperature of 473 K, a propionic acid gas phase partial pressure of 1 bar, a CO gas phase partial pressure of 1×10^{-5} bar, and a hydrogen partial pressure of 0.01 bar (Fig, S2), TOFs (s^{-1}) of various elementary steps on Pd(100) and Pd(111) in 1,4-dioxane with +10% increased palladium COSMO cavity radius at a temperature of 473 K, a propionic acid gas phase partial pressure of 1 bar, a CO gas phase partial pressure of 1×10^{-5} bar and a hydrogen partial pressure of 0.01 bar (Fig. S3), TOFs (s^{-1}) of various elementary steps in 1,4-dioxane with –10% decreased palladium COSMO cavity radius at a temperature of 473 K, a propionic acid gas phase partial pressure of 1 bar, a CO gas phase partial pressure of 1×10^{-5} bar, and a hydrogen partial pressure of 0.01 bar (Fig. S4) and different shapes of cluster sizes cut from Pd(100) surface, which are used in solvation calculations for HDO of propanoic acid on Pd(100), plot of CO adsorption energy on Pd(100) surface in liquid water vs. number of metal atoms in the respective cluster, 30×21 cluster model (consists of 51 Pd atoms) cut from Pd(111) surface used in solvation calculations for HDO of propanoic acid on Pd(111) (Fig. S5).

*Corresponding author email: heyden@cec.sc.edu

Phone: +1-803-777-5025

Abstract

Microkinetic models based on parameters obtained from density functional theory and transition state theory have been developed for the hydrodeoxygenation (HDO) of propanoic acid, a model lignocellulosic biomass-derived organic acid, over the flat Pd(100) and Pd(111) surfaces in both vapor and liquid phase reaction conditions. The more open Pd(100) surface was found to be 3-7 orders of magnitude more active than the Pd(111) surface in all reaction environments, indicating that the (111) surface is not catalytically active for the HDO of propanoic acid. Over Pd(100) and in vapor phase, liquid water, and liquid 1,4-dioxane, propanoic acid hydrodeoxygenation follows a decarbonylation (DCN) mechanism that is facilitated by initial α- and β-carbon dehydrogenation steps, prior to the rate controlling C-OH and (partially rate controlling) C-CO bond dissociations. Only over Pd(111) and aqueous reaction environments is the decarboxylation (DCX) preferred over the DCN with the C-CO_2 step being rate controlling.

Keywords

Hydrodeoxygenation, Surface structure sensitivity, Microkinetic modeling, Propanoic acid, Biomass conversion, DFT, Solvent effect, Lateral interaction.

1. Introduction

Biomass is a promising renewable resource that can strengthen the energy supply chain via efficient implementation in the global energy infrastructure. Catalytic conversion of biomass to biofuels is one potential route for its utilization. First-generation biofuels such as bioethanol and biodiesel contain oxygenates that are often not compatible with the current transportation infrastructure due to corrosion issues and a lower energy density than conventional hydrocarbon fuels.[1-5] Therefore, the production of oxygen-free hydrocarbons (second-generation biofuel, denoted as green diesel) from biomass feedstocks through catalytic hydrodeoxygenation (HDO) at moderate reaction conditions is one important research area awaiting breakthroughs.

The emergence of the food-*versus*-fuel debate has encouraged researchers to reduce edible biomass (such as corn or cane sugar) usage during biofuel production and develop new technologies to utilize non-edible biomass like lignocellulose, which is more abundant and can be grown faster and with lower costs.[2,6] Over the years, various conventional alumina supported hydrotreating catalysts, i.e., sulfided NiMo/Al_2O_3 and CoMo/Al_2O_3, have been used for the conversion of vegetable and pyrolysis oils to liquid hydrocarbons.[7,8] However, these traditional catalysts have difficulties with carbon oxides separation, high sulfur contents, and short lifespan, which interrupt their practical usage in large scale biofuel production.[7,8] Thus, it is essential to develop suitable catalysts for the HDO of various bio-oils (a mixture of highly oxygenated compounds, including acids, alcohols, esters, aldehydes, ketones, and aromatics),[9,10] obtained from, e.g., pyrolysis of lignocellulosic biomass.[2] Here, in particular, the HDO of organic acids is a slow process that requires improvements.

Among the various noble metal catalysts, palladium (Pd) has attracted considerable interest for the HDO of long-chain organic acids like lauric acid, palmitic acid, and stearic acid.[11-15] An early effort began about four decades ago when Maier and co-workers (1982) reported Pd/SiO_2 catalysts suitable for deoxygenation of carboxylic acids.[16] Murzin *et al.* and Boda et al. performed thorough investigations for transforming long-chain fatty acids to alkanes over carbon-supported palladium (Pd/C) catalysts and studied the preferred HDO mechanism among decarbonylation (DCN), decarboxylation (DCX), and reductive deoxygenation (RDO).[17,18] Overall, there is a desire to design more active and selective DCX or DCN catalysts in future biorefineries because RDO demands a larger supply of hydrogen from external fossil-fuel sources to remove oxygen in the form of water. This is, in particular, the case if alkanes, and not alcohols or aldehydes, are the target products. The DCN and DCX mechanisms require less hydrogen to remove oxygen in the form of CO_2 and CO, where CO is often transformed to CO_2 by the water-gas shift reaction. Lugo-José et al. explored the selective HDO of propanoic acid (PAc) over supported group VIII noble metals experimentally and concluded that turnover frequencies (TOFs) for the PAc conversion are highest over Pd-based catalysts.[19] Lugo-José et al. also evaluated the catalytic effect of the support, i.e., SiO_2, TiO_2, and carbon, for palladium catalysts and conferred that Pd/C is most selective (~90–100%) towards non-oxygenated alkane production via decarbonylation and decarboxylation over the entire temperature range of 200–400°C and that the carbon support does not participate in the observed catalytic activity.[19] In contrast, moderate to a strong interaction between the supports and the acid in SiO_2 and TiO_2 supported Pd catalysts led to the formation of oxygenated hydrocarbons (aldehyde, ketone) together with non-oxygenated hydrocarbons.[19] Given these experimental observations, we conclude that any computational study of the HDO of PAc over Pd catalysts that only considers the metal phase and not the support can only mimic Pd/C catalysts, and for these catalysts, only the DCN and DCX mechanisms need to be considered.

Even when neglecting support effects, supported Pd nanoparticle catalysts display various active Pd sites that can display very different activities and selectivities.[20-28] For very small nanoclusters, there can be strong particle size effects, and even for larger nanoparticles, the metal particle consists of surface atoms with different coordination (like steps, edges, kinks, and corners), leading to different electronic properties.[29,30] Boudart et al. ranked catalytic reactions as either structurally–sensitive or structurally–insensitive.[31] For a structurally sensitive reaction, the chemisorption energy and binding mode change significantly across the different faces of a metal crystal.[32,33] For Pd catalysts in general and for the deoxygenation of organic acids in particular, it has been argued that the fraction of (111) versus (100) versus (211) surface sites has a significant effect on a catalyst's activity and selectivity.[34-37] Assuming a cuboctahedral shape of catalyst particles with corners truncated as (100) planes and applying Van Hardeveld and Hartog statistics,[38] Lugo- José et al. estimated the fraction of each surface site j (i.e., (100), (111) and corners/edges) in a series of catalysts with different particle size distribution and concluded that for the HDO of PAc very small Pd clusters and corner and edge sites of larger Pd particles are significantly less active than the (111) and (100) sites of Pd particles.[39] This observation agrees with computational studies that also predict a low HDO activity over Pd(211).[40,41] Due to model approximations and experimental uncertainties, Lugo- José et al. could unfortunately not conclusively determine if (111) or (100) sites are significantly more active.

Based on these experimental observations, we have previously investigated the HDO of PAc over various closed-packed metal surfaces from first principles.[1,42-47] Our objective had been understanding the reaction mechanism and reaction kinetics with the ultimate goal of designing new transition metal catalysts for the HDO of organic acids. Our model reactant has been propanoic acid (PAc) since both experimental vapor and liquid phase studies can be conducted for

PAc and because it possesses an α-carbon –CH_2 group characteristic of long-chain organic acids, i.e., there is some hope that the results can be extrapolated to longer-chain hydrocarbons. A challenge of our calculations has consistently been that we predicted relatively low turnover frequencies (TOFs), which in principle could have its origin in model approximations such as the chosen lateral interaction model and approaches for modeling van-der-Waals interactions; however, it could also point to the (111) metal surface not being the active site in the experimental catalysts. Thus, one of the primary objectives of this article is to investigate the HDO of PAc over Pd(100) from first principles and determine whether the Pd(100) surface is more active than the Pd(111) surface and if experimental observations can be reproduced more reliably for this surface structure. Given that processing of vegetable and pyrolysis oils will likely have to occur in a condensed phase containing both significant amounts of water and/or less polar solvents, we also investigated the effects of liquid water and liquid 1,4-dioxane on the reaction rate and kinetic parameters. We note that experimentalists have already shown that solvents such as dodecane, mesitylene, and water not only increase the targeted product selectivity but also boost net rates of the HDO of organic acid and esters over supported metal catalysts.[11,17,47-51]

To summarize, this paper presents a careful density functional theory (DFT) study of various elementary reactions involved in the DCN and DCX mechanisms of PAc over Pd(100) and contrasts these results to our prior data obtained for the HDO of PAc over Pd(111). Moreover, a comprehensive microkinetic model is developed for the HDO of PAc over Pd(100) in a vapor, liquid water, and liquid 1,4-dioxane reaction environment. We consider lateral interaction effects on both adsorption and surface reactions to predict the dominant reaction pathway, rate-limiting elementary steps, and reaction orders. Given that such an elaborate lateral interaction model has previously not been used in our Pd(111) study, we also developed such a model for the HDO of

PAc over Pd(111). Overall, the same approximations have been applied for both Pd surface structures to maximize error cancellation.

2. Methods

2.1 Computational Models

Periodic plane-wave based DFT calculations have been performed with the Vienna Ab Initio Simulation Package (VASP)[52,53] to solve the Kohn-Sham equations under periodic boundary conditions and attain adsorption and transition state energies and vibrational properties of all chemical species of relevance for this investigation. The electron-ion interaction is modeled using the projector-augmented wave method (PAW).[54] The nonlocal generalized gradient Perdew and Wang 91 (PW91) functional is used to describe exchange and correlation, and a k-point mesh of $4 \times 4 \times 1$ is used for Brillouin-zone integration according to the Monkhorst-Pack scheme with a Methfessel-Paxton smearing of 0.2 eV.[55-58] An energy cutoff for plane waves of 400 eV and a self-consistent field (SCF) energy convergence criterion of 1×10^{-7} eV have been used throughout this study. All calculations are non-spin-polarized. The optimized lattice constant of fcc-Pd bulk (3.952 Å) is consistent with the experimental value of 3.891 Å. To avoid interactions between the slab and its periodic image, palladium layers in both structures are separated by a vacuum layer of 15 Å. Each Pd layer has 12 Pd atoms with $3\times2\sqrt{3}$ periodicity. The bottom two Pd layers are fixed to their bulk positions, while the top two layers are allowed to relax in all directions during optimization and transition state search calculations. For each elementary reaction step, transition state was determined climbing image nudged elastic band (CI-NEB) method followed by dimer method.[59-62] Lastly, all metal atoms are fixed in their optimized position during vibrational frequency calculations. To minimize the errors associated with the harmonic approximation for small frequencies, frequencies below 100 cm^{-1} are shifted to 100 cm^{-1} during partition function calculations.[44]

The approximate effect of solvents on reaction mechanisms at metal-liquid interfaces is studied using the implicit solvation model for solid surfaces (iSMS) method.[63] The main feature of this method is that it includes long-range metal interactions via periodic-slab calculations within the context of DFT calculations in the absence of a solvent and it considers the effect of the liquid as a localized perturbation that can be explained by cluster models embedded in an implicit continuum solvent. The free energy of an adsorbed intermediate on a periodic metal slab at the solid-liquid interface, $G^{liquid}_{surface + intermediate}$, is defined using a subtraction scheme:

$$G^{liquid}_{surface + intermediate} = G^{vacuum}_{surface + intermediate} + \left(G^{liquid}_{cluster + intermediate} - E^{vacuum}_{cluster + intermediate}\right) \quad (1)$$

where $G^{vacuum}_{surface + intermediate}$ is the plane wave DFT energy of the periodic slab model, including vibrational contributions to the free energy in the absence of a solvent, $G^{liquid}_{cluster + intermediate}$ is the free energy of a metal cluster in the liquid constructed by removing selected metal atoms from the periodic-slab model and removing the periodic boundary conditions, and $E^{vacuum}_{cluster + intermediate}$ is the DFT energy of the same cluster in the absence of the solvent. Cluster model DFT calculations were carried out using TURBOMOLE 7.2.1.[64-66] For solvation effect calculations, the lowest energy spin state has been identified by single point energy calculations on various spin surfaces for each two-layered cluster model (Figure S5) using the RI-J approximation with auxiliary basis sets and a self-consistent field energy convergence criterion of 1×10^{-7} Ha.[67-69] COSMO and COSMO-RS[70,71] implicit solvation models are used concurrently to calculate $G^{liquid}_{cluster + intermediate}$ using the COSMOtherm program on the same spin surface as for the vacuum cluster calculation.[72] The COSMOtherm database provides thermodynamic properties of the solvents based on quantum chemical COSMO calculations at the BP-TZVP level of theory.[64,73-76] COSMO-RS iSMS is a temperature-dependent solvent model that takes the effect of temperature on solvation into account.[70,71] Thus, COSMO-RS calculations were conducted at this level of theory for all structures at the relevant temperatures. Since the solvent parameters for the Pd metal atoms were uncertain, the solvent calculations were repeated with a cavity radius of $\pm10\%$ of the default Pd cavity. We can then examine the sensitivity of our liquid phase results to the most relevant Pd solvent parameter in this way.

2.2 Microkinetic Modeling

The free energy of reaction (ΔG_{Rxn_k}) and free energy of activation (ΔG_{TS_k}) of each elementary reaction step *k* were calculated according to the following equations –

$$\Delta G_{Rxn_k} = \sum_i v_{i_k} \times G_{ads,i_k} \tag{2}$$

$$\Delta G_{TS_k} = G_{TS_k} - \Sigma\, G^{R}_{ads,\,k} \tag{3}$$

where v_{i_k} and G_{ads,i_k} are the stoichiometric coefficients and adsorption energy of intermediates *i* in reaction step *k* and G_{TS_k} and $\Sigma G^{R}_{ads,\,k}$ are the transition state energies and the sum of the adsorption energies of reactants (R) in reaction step *k*, respectively. Adsorption free energies, G_{ads}, of all intermediates were calculated using the following equation –

$$G_{ads} = G_{surface+intermediate} - G_{surface} - (N_C \times E_C + N_H \times E_H + N_O \times E_O) \tag{4}$$

where $G_{surface+intermediate}$ is the free energy of the intermediate on the surface, $G_{surface}$ is the free energy of the clean surface slab, and E_C, E_H, and E_O are calculated from the total energies of CH_4, H_2O, and H_2 (E_{CH_4}, E_{H_2O}, and E_{H_2}), respectively, using the following equations –

$E_C = E_{CH_4} - 2 \times E_{H_2}$ --(5) $E_H = {}^{1}/_{2} \times E_{H_2}$ --(6) $E_O = E_{H_2O} - E_{H_2}$ --(7)

For surface reactions, the forward rate constant (k_{for}) has been calculated as

$$k_{for} = \frac{k_B T}{h} e^{-\frac{\Delta G_{TS}}{k_B T}} \tag{8}$$

where k_B is the Boltzmann constant, T is the reaction temperature in Kelvin, h is the Planck constant, and ΔG_{TS} is the free energy of activation for the forward reaction at a specific temperature. The reverse rate constant (k_{rev}) has been calculated similarly such that the thermodynamic equilibrium constant K is given as

$$K = \frac{k_{for}}{k_{rev}} \tag{9}$$

The forward rate constant of an adsorption reaction, A(g) + * ⇌ A*, is calculated by collision theory with an approximate sticking probability of 1 independent of reaction environment/solvent.[77]

$$k_{for} = \frac{1}{N_0\sqrt{2\pi m_a k_B T}} \tag{10}$$

where N_0 is the number of sites per area, which is $1.48\times10^{19}m^{-2}$ for Pd(111) and $1.28\times10^{19}m^{-2}$ for Pd(100). m_a denotes the molecular weight of A. Desorption rate constants are calculated from the adsorption equilibrium constant and the adsorption rate constant using equation 9. The free energy of reaction and free energy of activation in the presence of solvent was calculated as

$$\Delta G^{solv}_{TS_k} = \Delta G^{Gas}_{TS_k} + G^{solv}_{TS_k} - G^{solv}_{IS_k} \tag{11}$$

$$\Delta G^{solv}_{Rxn_k} = \Delta G^{Gas}_{Rxn_k} + G^{solv}_{FS_k} - G^{solv}_{IS_k} \tag{12}$$

where $G_{IS_k}^{solv}$, $G_{FS_k}^{solv}$ and $G_{TS_k}^{solv}$ are the solvation free energies of the initial, final, and transition states of reaction step k, respectively, which were obtained from the gas-phase cluster and COSMO-RS calculations. The free energy of adsorption for an adsorption reaction in solvent (ΔG_{ads}^{solv}) is calculated as

$$\Delta G_{ads}^{solv} = \Delta G_{ads}^{Gas} + G_{adsorbate}^{solv} - G_{Pd}^{solv} \tag{13}$$

where ΔG_{ads}^{Gas} is the free energy of adsorption under gas-phase conditions, and $G_{adsorbate}^{solv}$ and G_{Pd}^{solv} are, as before, the solvation free energies of the adsorbed molecule and the Pd surface immersed in the solvent, respectively. With defined forward and reverse rate constants, a full set of differential species equations for the normalized surfaces coverages of all reaction intermediates (normalized by surface metal atoms) have been solved until steady-state using MATLAB's ODE solver (ode15s). Thus, for a given reaction environment, temperature, fluid-phase fugacities, the surface coverage, rate of each intermediate reaction step, and turnover frequency are determined.

2.3. Lateral interaction effects

Adsorbate-adsorbate interactions can substantially influence the adsorption energy of surface intermediates and the stability of transition states.[38,39,47-49] Without considering lateral interactions in our mean-field microkinetic models, we observed that both the Pd(100) and Pd(111) surfaces were covered with CO and H ($\theta_{CO} + \theta_H > 98\%$), leading to very few free sites and small turnover frequencies. Hence, we considered the lateral interaction between all surface intermediates and the most abundant surface species (CO and H in this study) in our model to compute approximate differential adsorption energies. Previously, we used Grabow's model,[78] which is easy to implement and appropriate if lateral interactions only need to be considered for a few surface intermediates. Unfortunately, it is not practical when lateral interaction effects need to be considered for both surface species and transition states. Thus, we used a linear lateral interaction model that considers the interactions of all high surface coverage species on all surface intermediates and transition states.

$$G_{ads,i}(\theta_j) = G_{ads,i}(0) + a_{i,j} \times \theta_j \quad (14)$$

$$G_{ads,i}(\theta_1,\dots,\theta_n) = G_{ads,i}(0) + \sum_{j \neq i}^{n} a_{i,j} \times \theta_j \quad (15)$$

$$G_{a_k}(\theta_1,\dots,\theta_n) = G_{a_k}(0) + 0.5(G_{Rxn_k}(0) - G_{Rxn_k}(\theta_1,\dots,\theta_n)) \quad (16)$$

where $G_{ads,i}(0)$ and $G_{ads,i}(\theta_j)$ are adsorption free energies of species i at zero surface coverage and high surface coverage (θ_j) of the most abundant species j (CO and H), respectively. $a_{i,j}$ is the lateral interaction coefficient of species *j* concerning adsorbed intermediate species *i,* which is assumed to be constant throughout this research. $G_{a_k}(\theta_1,\dots,\theta_n)$ and $G_{a_k}(0)$ are the activation barriers of reaction step *k* at high and zero surface coverage of all other surface species j, respectively. The free energy of reaction of step *k* (G_{Rxn_k}) in the presence and absence of the most abundant species j can also be written as $G_{Rxn_k}(\theta_1,\dots,\theta_n) = \sum_i v_{i_k} \times G_{ads,i}(\theta_1,\dots,\theta_n)$ and $G_{Rxn_k}(0) = \sum_i v_{i_k} \times G_{ads,i}(0)$, where v_{i_k} is the stoichiometric coefficient of species *i* involved in reaction step *k*. We note that other functional forms for our lateral interaction model are possible; however, more complex forms require more DFT calculations; and all functional forms will produce similar results as long as the prediction coverage of the microkinetic model is similar to the coverage at which the lateral interaction model is parameterized. Fortunately, we choose to perform the lateral interaction calculations at 25% coverage which is for the strongest interacting surface species, CO, close to the actual coverage of ~20%. Therefore, our lateral interaction model should be reliable regardless of functional form.

3. Results and Discussion

Our investigated reaction network is identical with our previous studies from our research group for the HDO of propanoic acid over metal catalysts and consists of forty-one elementary reactions.[11-13] Figure 1 illustrates all elementary reaction steps and intermediates involved in the DCN and DCX of propanoic acid to produce C_2 hydrocarbons over different surface structures of Pd. As noted in the introduction, C-C cracking reactions and C_3 products are not considered since they are not observed experimentally for Pd/C catalysts. Reaction free energies (ΔG_{Rxn}) and activation free energy barriers (ΔG_{TS}) at a temperature of 473 K are shown in Table 1. Solvation effects of water and 1,4-dioxane to reaction energies ($\Delta\Delta G_{Rxn}$) and activation barriers ($\Delta\Delta G_{TS}$) are also presented in the same table.

In the following, we will first discuss the differences in microkinetic modeling results between the HDO of propanoic acid over Pd(100) and Pd(111) in a vapor phase reaction environment. Then, we present results in liquid water and liquid 1,4-dioxane reaction environments at otherwise identical reaction conditions. Finally, we will extend our discussions to the dominant pathways, the sensitivity of the adsorbed intermediates, rate-controlling steps, reaction orders, and apparent activation energies.

3.1 Microkinetic Modeling – Gas Phase

A microkinetic model is developed that contains all elementary reactions shown in Figure 1 at an experimental reaction temperature of 473 K. We used a one-site model that permits competition of every species with each other for space on the surface. Also, we considered that some surface species occupy more than one metal site. MATLAB code of our microkinetic models is shown in the Supporting Information. Next, we assumed differential conversion and partial pressures of propanoic acid, H_2O and CO_2 of 1 bar; although, the partial pressures of H_2O and CO_2 do not affect our results. For H_2, we used a typical partial pressure range of 0.01 – 10 bar. Most simulations are performed at 0.01 bar; however, we note that due to the PW91 predicted overbinding of hydrogen, this corresponds likely to a somewhat larger (although not precisely known) experimental hydrogen pressure. As we did not include the water-gas shift ($CO + H_2O \rightarrow CO_2 + H_2$) reaction in our models that converts the CO produced by DCN and since very small amounts of CO can significantly affect the HDO rate, we used a constant CO partial pressure of 1×10^{-5} bar except when otherwise noted. All other gas-phase product (ethane, ethene, and acetylene) partial pressures were set to zero. Without considering lateral interactions, we observed in all simulations a CO and H covered surface, and thus, we considered their lateral interactions with all other surface intermediates and transition states on both Pd(100) and Pd(111). Table S2 in the Supporting Information (SI) lists all lateral interaction parameters (a_{CO} and a_H) for Pd(100) and Pd(111). In the following, we define the turnover frequency (TOF) as the consumption rate of propanoic acid per surface Pd atom. Finally, we note that a palladium hydride (PdH) or a subsurface hydride phase can form in the presence of high-pressure hydrogen. However, at a low hydrogen partial pressure of 0.01 bar and a reaction temperature of 473 K, bulk PdH is not thermodynamically stable, so throughout this study, we did not consider the formation of a bulk or a subsurface PdH phase.[79]

Pd(100): The overall gas phase TOF for the HDO of PAc over Pd(100) was calculated to be 2.45×10^{-2} s^{-1} at 473 K, which is slightly larger than the experimentally observed TOF for the same reaction over a Pd/C catalyst[19] which was found to be 1.67×10^{-4} s^{-1} (0.01 min^{-1}). We note that the experimental rate is normalized to the total number of Pd surface atoms, while our rate is normalized to the number of Pd(100) surface atoms. Before further discussing the TOF and other kinetic data, we briefly discuss the reaction network for the HDO of PAc.

The DCN mechanism for the HDO of propanoic acid can occur through three major reaction pathways such as (a) the direct DCN without any dehydrogenation ($CH_3CH_2COOH \rightarrow CH_3CH_2CO \rightarrow CH_3CH_2 \rightarrow CH_3CH_3$), (b) complete α-carbon dehydrogenation before DCN ($CH_3CH_2COOH \rightarrow CH_3CHCOOH \rightarrow CH_3CCOOH \rightarrow CH_3CCO \rightarrow CH_3C \rightarrow CH_3CH \rightarrow CH_3CH_2 \rightarrow CH_3CH_3$), and (c) α- and β-carbon dehydrogenation ahead of the DCN ($CH_3CH_2COOH \rightarrow CH_3CHCOOH \rightarrow CH_2CHCOOH \rightarrow CHCHCOOH \rightarrow CHCHCO \rightarrow CHCH \rightarrow CH_2C \rightarrow CH_3C \rightarrow CH_3CH \rightarrow CH_3CH_2 \rightarrow CH_3CH_3$). At 473 K, the activation free energy for the direct dehydroxylation of propanoic acid (Step 1: $CH_3CH_2COOH^* + 2^* \rightarrow CH_3CH_2CO^{**} + OH^*$, ΔG_{TS} = 0.82 eV) is 0.32 eV higher than the free energy barrier for the α-carbon dehydrogenation (Step 2: $CH_3CH_2COOH^* + 2^* \rightarrow CH_3CHCOOH^{**} + H^*$, ΔG_{TS} = 0.50 eV). Subsequent α-carbon dehydrogenation of $CH_3CHCOOH^{**}$ (Step 7: $CH_3CHCOOH^{**} + {}^* \rightarrow CH_3CCOOH^{**} + H^*$, ΔG_{TS} = 0.73 eV) is not favored because it requires overcoming a higher activation free energy barrier than the preferred β-carbon dehydrogenation of $CH_3CHCOOH^{**}$ (Step 6: $CH_3CHCOOH^{**} + 2^* \rightarrow CH_2CHCOOH^{***} + H^*$, ΔG_{TS} = 0.42 eV). Then adsorbed vinyl-1-ol-1-olate ($CH_2CHCOOH$) preferentially undergoes dehydroxylation (Step 11: $CH_2CHCOOH^{***} + {}^* \rightarrow CH_2CHCO^{***} + OH^*$, ΔG_{TS} = 1.11 eV), β-carbon dehydrogenation (Step 16: $CH_2CHCO^{***} \rightarrow CHCHCO^{**} + H^*$, ΔG_{TS} = 0.51 eV) and decarbonylation (Step 18: $CHCHCO^{**} + {}^* \rightarrow CHCH^{**} + CO^*$, ΔG_{TS} = 0.90 eV) toward products. The microkinetic model (including lateral interactions) suggests the same dominant reaction pathway for the DCN of PAc over Pd(100) as a "thermodynamic study" would predict based on zero-coverage free energy, ΔG, calculations at 473 K (see Figure 1).

DCX pathways can also remove oxygen atoms in the form of CO_2. Four potentially relevant reaction pathways have been identified in DCX reaction mechanism: α- and β-carbon dehydrogenation before decarboxylation (DCX1: $CH_3CH_2COOH \rightarrow CH_3CHCOOH \rightarrow$

$CH_2CHCOOH \rightarrow CH_2CH \rightarrow\rightarrow$ products), O-H bond cleavage followed by partial or full α-carbon dehydrogenation and decarboxylation (DCX2: $CH_3CH_2COOH \rightarrow CH_3CH_2COO \rightarrow CH_3CHCOO \rightarrow CH_3CCOO \rightarrow CH_3C \rightarrow\rightarrow$ products), complete α-carbon dehydrogenation followed by C-C cleavage (DCX3: $CH_3CH_2COOH \rightarrow CH_3CHCOOH \rightarrow CH_3CCOOH \rightarrow CH_3C \rightarrow\rightarrow$ products) and O-H bond dissociation followed by decarboxylation (DCX4: $CH_3CH_2COOH \rightarrow CH_3CH_2COO \rightarrow CH_3CH_2 \rightarrow\rightarrow$ products). Among the different DCX pathways, DCX1 and DCX3 differ from others (DCX2 and DCX4) by their initial α-carbon dehydrogenation and C-C bond cleavage liberating a carboxylic group (COOH). Other pathways (DCX2 and DCX4) start with production of propanoate (CH_3CH_2COO) by O-H cleavage, and decarboxylation proceeds with C-CO_2 bond dissociation. C-C bond cleavage of the DCX1 route (2.56×10^{-5} s^{-1}) is preferred over the direct decarboxylation DCX4 route (2.29×10^{-6} s^{-1}) with an approximately one order of magnitude higher TOF. However, C-C bond cleavage from vinyl-1-ol-1-olate ($CH_2CHCOOH$) (Step 37: $CH_2CHCOOH^{***} + 2^{*} \rightarrow CH_2CH^{***} + COOH^{**}$, $\Delta G_{TS} = 1.37$ eV) involves overcoming a 0.26 eV higher activation barrier relative to the rate-limiting C-OH bond dissociation (Step 11: $CH_2CHCOOH^{***} + {}^{*} \rightarrow CH_2CHCO^{***} + OH^{*}$, $\Delta G_{TS} = 1.11$ eV) in the DCN. Thus, the turnover frequency of the DCX pathways is ~3 orders of magnitude lower (2.79×10^{-5} s^{-1}) at 473 K than the summation of the TOFs of the DCN pathways and the DCN selectivity is nearly 100% over Pd(100) and vapor phase reaction conditions.

Table 2 illustrates that at 473 K, the PAc conversion rate decreases by ~2 to 3 orders of magnitude when increasing the CO ($1\times10^{-5} - 1\times10^{-1}$ bar) and H_2 (0.01 – 10 bar) partial pressure in the vapor phase, primarily due to repulsive lateral interaction effects of adsorbed CO and H and site blockage of these species. Increasing the reaction temperature from 473 K to 523 K, increases the gas phase PAc conversion rate by a factor 3-5 times. Rate constants increase with temperature, and the CO and H coverage decreases (see Table 3). Interestingly, the free site coverage is not increasing with temperature due to accumulation of acetylene on the surface. Given that we did not consider lateral interaction of adsorbed acetylene with other surface species and transition state, the predicted acetylene coverage is likely an overestimation.

Pd(111): The overall gas-phase turnover frequency of PAc on Pd(111) is calculated to be 2.57×10^{-9} s^{-1}, which is approximately seven orders of magnitude lower than the TOF over Pd(100). CO adsorbs slightly stronger on Pd(111) relative to Pd(100) $\left(\text{Step 47:}\Delta G_{CO(Ads)}^{Pd(111)} = -0.46\ \text{eV vs}\ \Delta G_{CO(Ads)}^{Pd(100)} = -0.42\ \text{eV}\right)$ and H_2 is much stronger adsorbed on Pd(111) relative to Pd(100) $\left(\text{Step 48: }\Delta G_{H_2(Ads)}^{Pd(111)} = -0.25\ \text{eV vs}\ \Delta G_{H_2(Ads)}^{Pd(100)} = -0.04\ \text{eV}\right)$. Thus, the free site coverage (θ^*= 0.24) is smaller over Pd(111) than over Pd(100) (θ^*= 0.64), being one (minor) reason why the overall rate of reaction is lower over Pd(111) than over Pd(100) at 473 K (see Table 2).

Propanoic acid dehydroxylation followed by full α-carbon dehydrogenation and decarbonylation ($CH_3CH_2COOH \rightarrow CH_3CH_2CO \rightarrow CH_3CHCO \rightarrow CH_3CCO \rightarrow CH_3C \rightarrow\rightarrow CH_3CH_3$) is the thermodynamically dominant reaction path at 473 K (Table 1) with four consecutive bond dissociations, e.g. C-OH (Step 1: $CH_3CH_2COOH^* + 3^* \rightarrow CH_3CH_2CO^{***} + OH^*$; ΔG_{TS} = 1.18 eV), C-H (Step 4: $CH_3CH_2CO^{***} \rightarrow CH_3CHCO^{**} + H^*$; ΔG_{TS} = 0.91 eV), C-H (Step 9: $CH_3CHCO^{**} + 2^* \rightarrow CH_3CCO^{***} + H^*$, ΔG_{TS} = 0.94 eV) and C-CO (Step 14: $CH_3CCO^{***} \rightarrow CH_3C^* + CO^* + {}^*$, ΔG_{TS} = 0.34 eV), and a TOF of 1.84×10^{-9} s^{-1} (Figure 1). Among the other competitive DCN pathways, the $CH_3CH_2COOH \rightarrow CH_3CHCOOH \rightarrow CH_2CHCOOH \rightarrow CH_2CHCO \rightarrow CHCHCO \rightarrow CHCH \rightarrow\rightarrow CH_3CH_3$ route requires overcoming high activation free energies to dissociate the rate determining carbon-hydroxyl bond (Step 11: $CH_2CHCOOH^{***} + {}^* \rightarrow CH_2CHCO^{***} + OH^*$, ΔG_{TS} = 1.43 eV) and carbon-carbon (Step 18: $CHCHCO^{****} \rightarrow CHCH^{***} + CO^*$, ΔG_{TS} = 0.66 eV) bond. This route displays a three orders of magnitude lower TOF of 2.05×10^{-12} s^{-1} in the vapor phase. DCX starting with hydrogen cleavage from the O-H group (Step 28: $CH_3CH_2COOH^* + 2^* \rightarrow CH_3CH_2COO^{**} + H^*$; $\Delta G_{TS} = 0.47$ eV) and then direct decarboxylation (Step 29: $CH_3CH_2COO^{**} \rightarrow CH_3CH_2^* + CO_2^*$; $\Delta G_{TS} = 1.41$ eV) also seems competitive to the above mentioned dominant DCN pathway. Although the DCX of propanoic acid over Pd(111) $(\sum TOF_{DCX} = 7.23 \times 10^{-10}\ s^{-1})$ is 2.6 times slower than the DCN $(\sum TOF_{DCN} = 1.84 \times 10^{-9} s^{-1})$ and the predicted DCX selectivity is accordingly somewhat lower than the DCN selectivity (S_{DCX}:S_{DCN} = 28:72) during gas-phase HDO; the rate difference is hardly large enough to make conclusive statements given all model uncertainties.

Table 2 illustrates the effect of varying CO and H_2 partial pressures on the TOFs and surface coverages in the gas phase. Increasing the hydrogen partial pressure from 0.01 bar to 10 bar reduces the TOF for the HDO of PAc over Pd(111) by ~5-6 orders of magnitude due to a lower free site coverage and repulsive lateral interaction effects of the adsorbed H. Under these conditions, the direct decarboxylation ($CH_3CH_2COOH \rightarrow CH_3CH_2COO \rightarrow CH_3CH_2 \rightarrow\rightarrow$ products) is becoming the dominant deoxygenation pathway. In contrast, increasing the CO partial pressure from 1×10^{-5} to 1×10^{-1} bar increases (at high H_2 pressure) the TOF by ~2 to 4 orders of magnitude (Table 2) due to repulsive interactions of adsorbed CO with various species, which prohibits excessive adsorption of H atoms on the Pd(111) surface. We further discuss this point later when we compute gas-phase reaction orders and perform a sensitivity analysis. At lower H_2 pressure and elevated CO partial pressure ($P_{CO} \geq 0.1$ bar), CO blocks the surface and inhibits the HDO rate.

Finally, increasing the temperature from 473 K to 523 K leads to an increase in TOF by 1 to 2 orders of magnitude (Table 3). At higher temperatures, the direct decarboxylation ($CH_3CH_2COOH \rightarrow CH_3CH_2COO \rightarrow CH_3CH_2 \rightarrow\rightarrow$ products) is predicted to become the dominant mechanism over

Pd(111) ($S_{DCX} = 0.56$ at 523K vs. $S_{DCX} = 0.28$ at 473K). However, at all reaction temperatures and partial pressures, we predict that the Pd(100) surface is at least four orders of magnitude more active than the Pd(111) surface under vapor phase reaction conditions. Also, over Pd(100) the DCN selectivity always remains close to 1, and the preferred reaction pathway always remains: $CH_3CH_2COOH \rightarrow CH_3CHCOOH \rightarrow CH_2CHCOOH \rightarrow CH_2CHCO \rightarrow CHCHCO \rightarrow CHCH \rightarrow\rightarrow$ products.

3.2 Microkinetic Modeling – Liquid Phase

Solvent effects are approximated by modeling reactions at solid-liquid interfaces with the iSMS method. For reactions in aqueous phase environments, the water fugacity is increased from 1 bar to 14.17 bar which corresponds to the equilibrium water partial pressure of a dilute solution at 473 K ($x_{water} f^{L}_{water} = y_{water} P_{total} = p_{water}$, where x_{water} and y_{water} are mole fraction of water respectively in liquid mixture and vapor; f^{L}_{water} is fugacity of pure water at reaction temperature; P_{total} and p_{water} are system total pressure and water partial pressure, respectively). For reactions in liquid 1,4-dioxane the solvent fugacity is 4.45 bar. Table 1 depicts the solvation effect of water, protic solvent, and 1,4-dioxane, an aprotic solvent, on the free energy of reaction $\left(\Delta\Delta G^{solv}_{Rxn} = \Delta G^{solv}_{Rxn} - \Delta G^{Gas}_{Rxn}\right)$ and activation $\left(\Delta\Delta G^{solv}_{TS} = \Delta G^{solv}_{TS} - \Delta G^{Gas}_{TS}\right)$ of all elementary steps. Solvents can stabilize or destabilize the adsorption of intermediates and modify metal-adsorbate interactions. For example, liquid water stabilizes the propanoic acid adsorption by 0.29 eV on Pd(100) surface and by 0.20 eV on Pd(111) surface (Table 1). In the following sections, we described the effects of the solvent on the results of our microkinetic model for Pd(100) and Pd(111).

3.2.1 Liquid water

Pd(100): In presence of liquid water, the rate of the HDO of PAc over the Pd(100) surface becomes one order of magnitude lower (TOF_{water}=1.35×10^{-3} s^{-1}) than predicted for the gas phase study (TOF_{gas}= 2.45×10^{-2} s^{-1}) (Figure 2). Water increases the adsorption strength of CO and H by 0.25 eV and 0.32 eV, respectively, at 473 K (Table 1). Thus, CO and H are the most abundant surface intermediates (θ_{CO}= 0.32 and θ_{H}= 0.17) and the free site (water covered) coverage decreases to 0.38 (Table 5). For the DCN mechanism in water, the α-carbon dehydrogenation of PAc (Step 2: $CH_3CH_2COOH^* + 2^* \rightarrow CH_3CHCOOH^{**} + H^*$, ΔG_{TS}^{gas} = 0.50 eV, $\Delta\Delta G_{TS}^{water}$= -0.03) followed by the β-carbon dehydrogenation of ethylidene-1-ol-1-olate ($CH_3CHCOOH$) (Step 6: $CH_3CHCOOH^{**} + 2^* \rightarrow CH_2CHCOOH^{***} + H^*$, ΔG_{TS}^{gas} = 0.42 eV, $\Delta\Delta G_{TS}^{water} =$ -0.05 eV) are both slightly facilitated in liquid water relative to the gas phase. In contrast, C-OH bond cleavage from vinyl-1-ol-1-olate (Step 11: $CH_2CHCOOH^{***} + {}^* \rightarrow CH_2CHCO^{***} + OH^*$, ΔG_{TS}^{gas} = 1.11 eV, $\Delta\Delta G_{TS}^{water}$= +0.03 eV), which is rate determining, and C-CO bond dissociation (Step 18: $CHCHCO^{**} + {}^* \rightarrow CHCH^{**} + CO^*$, ΔG_{TS}^{gas} = 0.90 eV, $\Delta\Delta G_{TS}^{water}$ = +0.02 eV) are slightly inhibited in liquid water (Table 1) such that the turnover frequency is slightly lower ($\sum TOF_{water} = 9.97 \times 10^{-4}\, s^{-1}$ vs $\sum TOF_{gas} = 2.41 \times 10^{-2}\, s^{-1}$). Similar to the gas phase, the HDO of PAc over Pd(100) proceeds in water by α- and β-carbon dehydrogenation followed by dehydroxylation and decarbonylation ($CH_3CH_2COOH \rightarrow CH_3CHCOOH \rightarrow CH_2CHCOOH \rightarrow CH_2CHCO \rightarrow CHCHCO \rightarrow CHCH \rightarrow\rightarrow$ products). Other DCN pathways such as (a) the direct DCN without dehydrogenation ($CH_3CH_2COOH \rightarrow CH_3CH_2CO \rightarrow CH_3CH_2 \rightarrow\rightarrow$ products, $\sum TOF_{water}$= 1.94×10^{-5} s^{-1}), (b) the complete α-carbon dehydrogenation and dehydroxylation before DCN ($CH_3CH_2COOH \rightarrow CH_3CHCOOH \rightarrow CH_3CHCO \rightarrow CH_3CCO \rightarrow CH_3C \rightarrow\rightarrow$ products, $\sum TOF_{water}$= 2.23×10^{-4} s^{-1}) are not favored under these reaction condition (Figure 2). Among the DCX pathways, O-H bond dissociation followed by direct decarboxylation ($CH_3CH_2COOH \rightarrow CH_3CH_2COO \rightarrow CH_3CH_2$

→→ products, $\sum \mathrm{TOF_{water}} = 3.98 \times 10^{-5}\ \mathrm{s}^{-1}$) is kinetically favorable. Figure 2 and Table 4 illustrate that the DCN mechanism remains dominant in liquid water and the selectivity towards decarboxylation increases only minimally ($\sum \mathrm{TOF^{DCN}_{water}} = 1.35\times10^{-3}$ $\mathrm{s^{-1}}$, $\mathrm{S^{water}_{DCN}} = 0.97$ vs $\sum \mathrm{TOF^{DCX}_{water}} = 4.13\times10^{-5}$ $\mathrm{s^{-1}}$, $\mathrm{S^{water}_{DCX}} = 0.03$). Even a variation in default palladium COSMO cavity radius by ±10% does not change the dominant mechanism for the HDO of PAc over Pd(100) and the TOF and selectivity change only minimally (Figure S1 and S2). Furthermore, Table 5 and 6 demonstrate that increasing the partial pressure of CO and H_2 or increases the temperature leads over Pd(100) in liquid water qualitatively to the same rate inhibition/increases as predicted for the vapor phase.

Pd(111): Liquid water increases the TOF of the HDO of PAc over Pd(111) by one order of magnitude (Figure 2) relative to the gas phase ($\mathrm{TOF_{water}} = 1.30\times10^{-8}\ \mathrm{s^{-1}}$ vs $\mathrm{TOF_{gas}} = 2.57\times10^{-9}\ \mathrm{s^{-1}}$). Water strongly stabilizes adsorbed CO ($\Delta\Delta \mathrm{G^{water}_{CO(Ads)}} = -0.24$) such that it covers nearly 70% of the surface sites at 473 K ($\theta^{\mathrm{water}}_{\mathrm{CO}} = 0.70$ vs $\theta^{\mathrm{gas}}_{\mathrm{CO}} = 0.21$), reducing the hydrogen coverage over Pd(111) ($\theta^{\mathrm{water}}_{\mathrm{H}} = 0.01$ vs $\theta^{\mathrm{gas}}_{\mathrm{H}} = 0.55$) (Table 3 and 5). Also, the dominant pathway changes over Pd(111) in presence of water in that the direct decarboxylation becomes the dominant mechanism (CH_3CH_2COOH →CH_3CH_2COO → CH_3CH_2 →→ products) instead of the decarbonylation with C-H bond activation that is preferred in the gas phase: PAc → dehydroxylation → full α-carbon dehydrogenation → decarbonylation → C_2 products. Liquid water facilitates the O-H bond activation (Step 28: $CH_3CH_2COOH^* + 2^*$ → $CH_3CH_2COO^{**} + H^*$; $\Delta \mathrm{G^{gas}_{TS}} = 0.47$ eV, $\Delta\Delta \mathrm{G^{water}_{TS}} = -0.02$ eV) and C-CO_2 bond dissociation (Step 29: $CH_3CH_2COO^{**}$ → $CH_3CH_2^* + CO_2^*$; $\Delta \mathrm{G^{gas}_{TS}} = 1.41$ eV, $\Delta\Delta \mathrm{G^{water}_{TS}} = -0.05$ eV) (see Table 1) and thus, the turnover frequency is increased ($\sum \mathrm{TOF_{water}} = 1.28\times10^{-8}\ \mathrm{s^{-1}}$ vs $\sum \mathrm{TOF_{gas}} = 7.23\times10^{-10}\ \mathrm{s^{-1}}$) and the selectivity dramatically changes to decarboxylation ($\mathrm{S^{water}_{DCX}} = 0.99$ vs $\mathrm{S^{gas}_{DCX}} = 0.03$) (Table 4).

We note that liquid water also reduces the selectivity to decarbonylation over Pd(111); however, the selectivity difference is large enough on the (100) facet that the effect is less pronounced ($S_{DCX\,(111)}^{water}/S_{DCN\,(111)}^{water} = 99$ vs $S_{DCX\,(100)}^{water}/S_{DCN\,(100)}^{water} = {}^{3}/_{97}$) (see Table 4). Figure S1 and S2 in the supporting information illustrates the complete reaction network, dominant pathway, rates and TOFs when changing the default palladium COSMO cavity radius by ±10% in lqiud water. Finally, Table 5 illustrate that increasing the CO and H_2 partial pressure decreases the TOF by 3 – 5 orders of magnitude in liquid water similar to the vapor phase simulations. Also, temperature increases lead to similar (although slightly larger) (factor 100) rate increases in liquid water (Table 6) as observed in the vapor phase. The relative increase in rate in water can be understood by the higher CO coverage in water and a higher temperature facilitating CO desorption. Finally, regardless of temperature, pressure, and changes in the default palladium COSMO cavity radius, the direct decarboxylation route is preferred in water, and the gas-phase-favored decarbonylation pathway is no longer dominant.

3.2.2 Liquid 1,4-dioxane

Pd(100): Overall TOF on Pd(100) in presence of aprotic solvent 1,4-dioxane is 7.15×10^{-4} s^{-1} (Figure 3), which is approximately one order of magnitude lower than gas phase and only by a factor of 2 lower than liquid water. However, the dominant mechanism of the HDO of propanoic acid over Pd(100) remains similar in 1,4-dioxane (Figure 3) to the gas and liquid water phase: α and β-carbon dehydrogenation → dehydroxylation → decarbonylation →→ products ($CH_3CH_2COOH \rightarrow CH_3CHCOOH \rightarrow CH_2CHCOOH \rightarrow CH_2CHCO \rightarrow CHCHCO \rightarrow CHCH \rightarrow\rightarrow$ products) and the DCN selectivity remains high ($S_{DCN}^{1,4-\mathrm{dioxane}} = 0.99$) (see Table 4). As before, increasing the CO (P_{CO}= 10^{-5} – 10^{-1} bar) and H_2 ($P_{H_2} = 0.01 - 10$ bar) partial pressures in 1,4-dioxane (Table 7) decreased the rate; and increasing the temperature increases the rate without a significant change in selectivity relative to our simulations for the Pd(100) surface in gas and liquid water reaction environments (Table 6). Finally, we found that the above mentioned dominant pathways and selectivity trends (S_{DCN} > S_{DCX}) remain identical when changing the default palladium COSMO cavity radius by ±10% for the simulations in 1,4-dioxane (see Figure S3 and S4).

Pd(111): In 1,4-dioxane, the HDO rate of PAc (TOF = 1.44×10^{-7} s^{-1}) is approximately one order of magnitude higher than in water and two orders of magnitude higher than in the vapor phase. In contrast to the simulations in liquid water, the DCN mechanism is preferred in 1,4-dioxane ($S_{DCN}^{1,4-\text{dioxane}} = 0.79$) and starts with dehydroxylation followed by α and β-carbon dehydrogenation ($CH_3CH_2COOH \rightarrow CH_3CH_2CO \rightarrow CH_3CHCO \rightarrow CH_2CHCO \rightarrow CH_2CH \rightarrow\rightarrow$ products) (Figure 3). Table 4 (and Figure S3 and S4) illustrate the sensitivity of the selectivity when changing the Pd cavity radius. Similar to our simulations in liquid water, increasing the partial pressures of CO and H_2 in 1,4-dioxane leads to a very small number of free sites, and the rate of reaction decreases by 2 – 6 order of magnitudes (Table 7). Increasing the reaction temperature increases the free site coverage and increases the reaction rate by ~2 orders of magnitude (for a 50 K increase – see Table 6).

4. Apparent Activation Barrier, Reaction Orders, and Sensitivity Analysis

To gain further insights into the temperature dependence of the conversion rate, the apparent activation barriers (E_{app}) have been calculated using Equation 17. Here, a temperature range of 473 to 523 K is used for all reaction environments and hydrogen partial pressures/fugacities.

$$E_{app} = k_B T^2 \left(\frac{\partial \ln(\text{TOF})}{\partial T}\right)_{P,p_i} \qquad (17)$$

Next, reaction orders were calculated at 473 K using Equation 18.

$$n_i = \left(\frac{\partial \ln(\mathrm{TOF})}{\partial \ln p_i}\right)_{T, p_{j,\ j \neq i}} \tag{18}$$

For the sensitivity analysis, Campbell's degrees of rate and thermodynamic rate control, $X_{RC,i}$ and $X_{TRC,n}$ and degrees of selectivity control (DSC_i) were calculated to identify rate- and selectivity-controlling steps and intermediates in the HDO of propanoic acid over Pd(100) and Pd(111).[43-47] Specifically, the following equations are used:

$$X_{RC,i} = \left(\frac{\partial \ln \mathrm{TOF}}{\partial \frac{-G_i^{TS}}{k_B T}}\right)_{G_{j \neq i}^{0,TS},\, G_m^0} \quad , \quad X_{TRC,n} = \left(\frac{\partial \ln \mathrm{TOF}}{\partial \frac{-G_n^{0}}{k_B T}}\right)_{G_{m \neq n}^{0},\, G_i^{0,TS}}$$

$$DSC_i = \left(\frac{\partial \ln S}{\partial \frac{-G_i^{TS}}{RT}}\right)_{G_{j \neq i}^{TS},\, G_m^0} = \left(\frac{\partial \ln \left(r_p / r_r\right)}{\partial \frac{-G_i^{TS}}{RT}}\right)_{G_{j \neq i}^{0,TS},\, G_m^0} = X_{RC,i\ P} - X_{RC,i\ R} \tag{19}$$

where G_j^{TS} and G_m^0 are the free energies of the transition state of reaction j and the ground state of intermediate m, respectively. Non-zero rate and selectivity control values indicate that the transition and ground states significantly influence the overall conversion of propanoic acid. The degree of selectivity control is an extended definition of the degree of rate control where the net rate is replaced with selectivity for the production of the most desired product P (C_2 hydrocarbons – CH_3CH_3 and CH_2CH_2) from the consumption of the most valuable reactant R (CH_3CH_2COOH)

, $S = {}^{r_p}/_{r_r}$. Here, DSC_i explains the relative increase in net selectivity to product P (ethane and ethylene) from reactant R (propanoic acid) due to the (differential) stabilization of the standard-state free energy for a transition state of reaction step i, holding all other transition states' and all adsorbed species' energies constant. $X_{RC,i\,P}$ and $X_{RC,i\,R}$ are the degrees of rate control of transition state i for the rates of making product P and consuming reactant R, respectively.

Pd(100): Our model predicts an apparent activation barrier (E_{app}) of +0.59 eV for the HDO of propanoic acid on Pd(100) in the gas phase (Figure 4), which is in reasonable agreement with experimentally observed E_{app} value of ~0.72±0.03 eV (16.7±0.6 kcal/mol).[19] The calculated apparent activation barriers in water (E_{app}^{water}) and 1,4-dioxane ($E_{app}^{1,4-dioxane}$) are +1.54 eV and +1.80 eV, respectively. The reaction order of propanoic acid in the gas phase and in a partial pressure range of 0.90–1.10 bar at 473K is +0.65 (Figure 5a), which is consistent with experimental studies ($n_{PAc} = 0.50$) by Lugo José et al.[23] As shown in Figure 5a, the reaction order of propanoic acid in water and 1,4-dioxane are +0.34 and +0.88, respectively. The reaction order of hydrogen (Figure 5b) is found to be –0.41 in gas, –0.46 in water, and –1.19 in 1,4-dioxane. This observation disagrees somewhat with experimental results that suggest the HDO of propanoic acid in gas phase is independent of partial pressure of hydrogen ($n_{H_2} = 0$).[19] Possibly, this difference in experimental and computational results originates from the use of the PW91 functional that overestimates hydrogen adsorption energies. Finally, in the CO partial pressure range of 10^{-6} – 10^{-4} bar, the calculated CO reaction order in gas, water, and 1,4-dioxane are –0.36, –0.76 and –0.37 (Figure 5c). In other words, CO poisons the surface, and whenever the DCN is the dominant reaction mechanism, it is imperative that the catalyst also catalyzes the water-gas shift reaction to reduce the CO partial pressure. Overall, Pd(100) is predicted to be an active catalyst at low hydrogen and CO partial pressure.

According to Campbell's degree of rate control, C-OH bond dissociation is the most rate-controlling step under both vapor and liquid phase conditions. As shown in Table 8, dehydroxylation of $CH_2CHCOOH$ (Step 11: $CH_2CHCOOH^{***} + {}^{*} \rightarrow CH_2CHCO^{***} + OH^{*}$, $X_{RC}^{gas} = 0.47$, $X_{RC}^{water} = 0.66$, $X_{RC}^{1,4-dioxane} = 0.81$) has the largest rate control value in all reaction environments – vapor and liquid. Additionally, α– and β– carbon dehydrogenation steps are also found to be partially rate-controlling under above-mentioned reaction conditions. X_{RC} of propanoic acid α– carbon dehydrogenation (Step 2: $CH_3CH_2COOH^{*} + 2^{*} \rightarrow CH_3CHCOOH^{**} + H^{*}$) are 0.18, 0.02 and 0.07 in gas, water and 1,4-dioxane, respectively. X_{RC} values of other major reaction steps are listed in Table 8.

The degree of thermodynamic rate control (X_{TRC}) of the two most abundant surface intermediates, CO^{*} and H^{*}, are listed in Table 9. In gas phase, the degrees of thermodynamic rate control of CO^{*} ($X_{TRC,\,CO} = -1.55$) and H^{*} ($X_{TRC,\,H} = -1.14$) suggest that the destabilization of CO^{*} and H^{*} can increase rate of reaction by creating free sites for the rate controlling step. In liquid phase reaction environments, the X_{TRC} of CO^{*} and H^{*} are: $X_{TRC,\,CO}^{water} = -3.23$, $X_{TRC,\,CO}^{1,4-dioxane} = -1.82$ and $X_{TRC,\,H}^{water} = -4.10$, $X_{TRC,\,H}^{1,4-dioxane} = -1.33$ respectively and the overall HDO rate can be improved by destabilizing both species. Table 10 illustrates degrees of selectivity control for the DCX and DCN pathways. Results indicate that the selectivity of the DCN path is entirely determined by C-OH bond dissociation (Step 11: $CH_2CHCOOH^{***} + {}^{*} \rightarrow CH_2CHCO^{***} + OH^{*}$, $DSC_{DCX}^{gas} = -0.92$, $DSC_{DCX}^{water} = -0.68$ and $DSC_{DCX}^{1,4-dioxane} = -0.83$) and to some extent on initial α–carbon dehydrogenation of PAc (Step 2: $CH_3CH_2COOH^{*} + 2^{*} \rightarrow CH_3CHCOOH^{**} + H^{*}$; $DSC_{DCX}^{gas} = -0.03$, $DSC_{DCX}^{water} = -0.03$ and $DSC_{DCX}^{1,4-dioxane} = -0.01$). In addition, a positive degree of selectivity control (DSC_{DCX}) is observed for the direct decarboxylation of propanoate (Step 29: $CH_3CH_2COO^{**} \rightarrow CH_3CH_2^* + CO_2^*$; DSC_{DCX}^{gas} = +0.08, DSC_{DCX}^{water}= +0.96 and $DSC_{DCX}^{1,4-dioxane}$= +0.95), demonstrating that stabilizing the C-CO_2 bond dissociation transition state increases the selectivity towards the DCX in all reaction environments.

Pd(111): An identical apparent activation energy trend $\left(E_{app}^{1,4-dioxane} > E_{app}^{water} > E_{app}^{gas}\right)$ is observed between Pd(100) and Pd(111). E_{app} for Pd(111) are 1.61 eV, 1.92 eV and 2.07 eV in gas, water, and 1,4-dioxane, respectively. For Pd(111), we observe that the propanoic acid, CO and H_2 reaction orders are a strong function of reaction environment (although in all environments the rate is extremely low) (see Figure 5). The propanoic acid reaction order is +1.0 in gas, +0.83 in water, and -0.29 in 1,4-dioxane and the H_2 order is generally negative, varying from -0.46 in water to -2.24 in the gas phase. Adsorbed hydrogen atoms inhibit the HDO of PAc on the (111) surface ($\theta_H^{gas} = 0.55$, $X_{TRC,\,H}^{gas} = -3.49$; $\theta_H^{water} = 0.01$, $X_{TRC,\,H}^{water} = -1.17$; $\theta_H^{1,4-dioxane} = 0.06$, $X_{TRC,\,H}^{1,4-dioxane} = -1.44$) and H^* adsorbed strongly in gas phase. The reaction order and X_{TRC} of CO^* in gas phase are +1.70 (Figure 5c) and +1.98, respectively, and demonstrate that adsorbed CO increases the TOF (Table 2). The only exception is at higher CO partial pressure ($\geq$ 0.1 bar) when CO occupies most of the surface sites ($\theta_{CO}^{gas} \geq 0.90$) and the TOF is reduced. Unlike the gas phase, negative reaction orders ($n_{CO}^{water} = -0.94$ and $n_{CO}^{1,4-dioxane} = -0.59$) and negative thermodynamic rate control values ($X_{TRC,\,CO}^{water} = -0.82$ and $X_{TRC,\,CO}^{1,4-dioxane} = -0.85$) were computed for CO^* in liquid phase due to its high surface coverage ($\theta_{CO}^{water} = 0.70$ and $\theta_{CO}^{1,4-dioxane} = 0.63$) even at low CO partial pressures.

Campbell's degree of rate control analysis (Table 8) suggests that propanoic acid dehydroxylation (Step 1: $CH_3CH_2COOH^* + 3^* \rightarrow CH_3CH_2CO^{***} + OH^*$; $X_{RC}^{gas} = 0.71$ and $X_{RC}^{water} = 0.01$) is rate controlling in gas phase and C-CO_2 bond breakage (Step 29: $CH_3CH_2COO^{**} \rightarrow CH_3CH_2^{*} + CO_2^{*}$; $X_{RC}^{gas} = 0.28$ and $X_{RC}^{water} = 0.98$) is rate controlling in liquid water. In 1,4-dioxane, hydrogenation of ethylidene (Step 25:$CH_3CH^{**} + H^{*} \rightarrow CH_3CH_2^{*} + 2^{*}$, $X_{RC} = 0.97$) is rate controlling in addition to C-OH bond cleavage in step 1 ($X_{RC} = 0.14$), while the degree of rate control value of C-CO_2 bond dissociation in step 29 is -0.22. Table 10 illustrates that C-OH bond dissociation determines the selectivity for the DCN (Step 1: $CH_3CH_2COOH^{*} + 3^{*} \rightarrow CH_3CH_2CO^{***} + OH^{*}$, DSC_{DCX}^{gas}= -0.71, DSC_{DCX}^{water}= 0.00 and $DSC_{DCX}^{1,4-\text{dioxane}}$= -0.12) and C-$CO_2$ bond dissociation dictates the selectivity of the DCX route (Step 29: $CH_3CH_2COO^{**} \rightarrow CH_3CH_2^{*} + CO_2^{*}$, DSC_{DCN}^{gas}= -0.29, DSC_{DCN}^{water}= -0.98 and $DSC_{DCN}^{1,4-\text{dioxane}}$= -0.22) for the HDO of PAc on the Pd(111) surface.

Finally, we note here that in liquid water, propanoic acid may, dependent on the solution pH, dissociate into a carboxylate that can adsorb and initiate the decarbonylation and decarboxylation reaction over Pd(100) and Pd(111). However, our simulation results in liquid water are hardly affected by the presence of the carboxylate species since the O-H bond dissociation is fast and kinetically not relevant over Pd(100) and Pd(111). As mentioned above, in liquid water, C-OH and C-CO_2 are rate limiting over Pd(100) and Pd(111) surfaces, respectively.

5. Conclusion

In conclusion, a microkinetic model with embedded lateral interactions was built from first principles to analyze the sensitivity of the surface structures (Pd(100) and Pd(111) towards the hydrodeoxygenation of propanoic acid in vapor, liquid water, and liquid 1,4-dioxane. The model strongly suggests that, in the gas phase, the hydrodeoxygenation of propanoic acid is structure sensitive and that the TOFs are significantly higher (by 6 to 7 orders of magnitude) over Pd(100) than over Pd(111). Similarly in condensed phase media, the Pd(100) surface is four to five orders of magnitude more active than the Pd(111) surface. Decarbonylation is the most dominant reaction mechanism on Pd(100) in all reaction environments and involves α- and β-carbon dehydrogenation steps prior to dehydroxylation, further β-carbon dehydrogenation and decarbonylation ($CH_3CH_2COOH \rightarrow CH_3CHCOOH \rightarrow CH_2CHCOOH \rightarrow CH_2CHCO \rightarrow CHCHCO \rightarrow CHCH \rightarrow\rightarrow CH_3CH_3/CH_2CH_2$). Although the decarbonylation is favored on Pd(100) in all reaction environments, the TOF values are different in each reaction environment and follow the sequence $TOF_{gas} > TOF_{water} > TOF_{1,4\text{-dioxane}}$. Over the Pd(111) surface in gas phase, the dominant decarbonylation reaction pathway begins with C-OH bond dissociation followed by full α-carbon dehydrogenation and decarbonylation ($CH_3CH_2COOH \rightarrow CH_3CH_2CO \rightarrow CH_3CHCO \rightarrow CH_3CCO \rightarrow CH_3C \rightarrow\rightarrow CH_3CH_3$ and CH_2CH_2). In the presence of liquid water, decarboxylation is preferred over decarbonylation with rate limiting C-CO_2 bond dissociation. Here, the overall reaction rate is ~1 order of magnitude higher than in the gas phase.

Finally, our sensitivity analysis suggests that stabilization of the rate controlling C-OH bond dissociation from vinyl-1-ol-1-olate ($CH_2CHCOOH$) may increase the overall rate of reaction and selectivity of DCN in gas and condensed phase media over Pd(100). Meanwhile, C-OH and C-CO_2 are rate and selectivity controlling in gas phase and liquid water over Pd(111). Overall, a reasonable agreement with the experimental turnover frequencies, dominant pathways, rate determining steps, apparent activation energies, and reaction orders could be achieved.

Conflicts of interest

There are no conflicts to declare.

Acknowledgments

The National Science Foundation funded this work under Grant No. DMREF-1534260 (most gas-phase calculations and models) and OIA-1632824 (most liquid phase calculations). This work was also partially supported by the South Carolina State Center for Strategic Approaches to the Generation of Electricity (SAGE). Computing resources have been provided by the National Energy Research Scientific Computing Center (NERSC) supported by the Office of Science of the U.S. Department of Energy, Extreme Science and Engineering Discovery Environment (XSEDE) by the Texas Advanced Computing Center (TACC) at the University of Texas at Austin (Grant no. TG-CTS090100), the Environmental Molecular Sciences Laboratory (EMSL) under the Pacific Northwest National Laboratory (PNNL) via the CASCADE clusters, and the University of South Carolina's High Performance Computing (HPC) Group.

Table 1. Reaction and activation free energies in eV of all the elementary reaction steps in the HDO of propanoic acid over Pd(100) and Pd(111) at a temperature of 473 K, a propanoic acid partial pressure of 1 bar, a CO partial pressure of 1×10^{-5} bar, and a hydrogen partial pressure of 0.01 bar in the vapor phase. Solvation free energy of reaction and activation are also given for both liquid water and 1,4-dioxane. The number of * symbolizes the number of occupied adsorption sites.

#	Facet	Surface reactions	Gas		Water		1,4-dioxane	
			ΔG_{Rxn} (eV)	ΔG_{TS} (eV)	$\Delta\Delta G^{water}_{Rxn}$ (eV)	$\Delta\Delta G^{water}_{TS}$ (eV)	$\Delta\Delta G_{Rxn}$ (eV)	$\Delta\Delta G_{TS}$ (eV)
0	100	$CH_3CH_2COOH(g)$ + * → CH_3CH_2COOH*	0.78	N/A	-0.29	N/A	-0.17	N/A
	111	$CH_3CH_2COOH(g)$ + * → CH_3CH_2COOH*	0.63	N/A	-0.20	N/A	-0.13	N/A
1	100	CH_3CH_2COOH* + 2* → CH_3CH_2CO** + OH*	0.02	0.82	-0.10	-0.02	-0.03	0.01
	111	CH_3CH_2COOH* + 3*→ CH_3CH_2CO*** + OH*	0.89	1.18	0.03	-0.02	0.07	0.03
2	100	CH_3CH_2COOH* + 2* → $CH_3CHCOOH$** + H*	-0.01	0.50	-0.17	-0.03	-0.07	0.01
	111	CH_3CH_2COOH* + 2* → $CH_3CHCOOH$** + H*	0.71	1.02	-0.01	-0.04	0.02	0.01
3	100	CH_3CH_2CO** → CH_3CH_2* + CO*	-0.06	1.06	-0.10	0.00	-0.05	-0.01
	111	CH_3CH_2CO*** → CH_3CH_2* + CO* + *	-0.51	1.41	-0.18	0.00	-0.11	0.01
4	100	CH_3CH_2CO** + * →CH_3CHCO** + H*	0.26	0.87	-0.18	-0.02	-0.10	0.00
	111	CH_3CH_2CO*** → CH_3CHCO** + H*	0.07	0.91	-0.10	-0.06	-0.04	-0.01
5	100	$CH_3CHCOOH$** + * → CH_3CHCO** + OH*	0.28	0.81	-0.11	-0.01	-0.06	-0.01
	111	$CH_3CHCOOH$** + * → CH_3CHCO** + OH*	0.26	0.79	-0.06	-0.05	0.00	-0.02
6	100	$CH_3CHCOOH$** + 2* → $CH_2CHCOOH$*** + H*	-0.43	0.42	-0.19	-0.05	-0.12	-0.02
	111	$CH_3CHCOOH$** + 2* → $CH_2CHCOOH$*** + H*	-0.74	0.36	-0.07	-0.05	-0.03	0.01
7	100	$CH_3CHCOOH$** + * → CH_3CCOOH** + H*	0.12	0.73	-0.18	-0.07	-0.13	-0.05
	111	$CH_3CHCOOH$** + 2* → CH_3CCOOH*** + H*	0.00	1.15	-0.11	-0.07	-0.08	-0.02
8	100	CH_3CHCO** → CH_3CH* + CO*	-0.30	1.05	-0.09	0.07	-0.06	0.04
	111	CH_3CHCO** + * → CH_3CH** + CO*	-0.56	1.17	-0.12	0.05	-0.08	0.02
9	100	CH_3CHCO** + * → CH_3CCO** + H*	0.04	0.62	-0.12	-0.01	-0.06	0.02
	111	CH_3CHCO** + 2* → CH_3CCO*** + H*	0.23	0.94	-0.04	-0.03	-0.03	-0.02
10	100	CH_3CHCO** + 2* → CH_2CHCO*** + H*	0.07	0.73	-0.19	-0.04	-0.11	0.00
	111	CH_3CHCO** + 2* → CH_2CHCO*** + H*	-0.04	0.71	-0.01	-0.04	0.01	0.00
11	100	$CH_2CHCOOH$*** + * → CH_2CHCO*** + OH*	0.78	1.11	-0.10	0.03	-0.05	0.01
	111	$CH_2CHCOOH$*** + * → CH_2CHCO*** + OH*	0.95	1.43	0.00	-0.05	0.04	-0.01
12	100	$CH_2CHCOOH$*** + * → CHCHCOOH*** + H*	0.57	1.05	-0.19	-0.05	-0.13	-0.04
	111	$CH_2CHCOOH$*** + * → CHCHCOOH*** + H*	0.50	1.13	-0.06	-0.02	-0.03	0.00
13	100	CH_3CCOOH** + * → CH_3CCO** + OH*	0.20	1.64	-0.05	0.03	0.01	0.03
	111	CH_3CCOOH*** + * → CH_3CCO*** + OH*	0.48	0.92	0.01	0.00	0.05	0.04
14	100	CH_3CCO** → CH_3C* + CO*	-0.80	0.68	-0.17	-0.07	-0.12	-0.05
	111	CH_3CCO*** → CH_3C* + CO* + *	-1.69	0.34	-0.14	0.02	-0.08	0.02
15	100	CH_2CHCO*** + * → CH_2CH*** + CO*	-0.36	0.74	-0.20	-0.03	-0.14	-0.02
	111	CH_2CHCO*** + * → CH_2CH*** + CO*	-0.54	1.01	-0.20	-0.01	-0.13	0.00
16	100	CH_2CHCO*** → CHCHCO** + H*	-0.12	0.51	-0.20	-0.03	-0.13	-0.02
	111	CH_2CHCO*** + 2* → CHCHCO**** + H*	0.51	0.97	-0.06	-0.03	-0.04	-0.02
17	100	CHCHCOOH*** → CHCHCO** + OH*	0.09	0.88	-0.11	0.01	-0.05	0.02
	111	CHCHCOOH*** + 2* → CHCHCO**** + OH*	0.96	1.28	0.00	0.00	0.03	0.02
18	100	CHCHCO** + * → CHCH** + CO*	-0.75	0.90	-0.14	0.02	-0.11	0.01
	111	CHCHCO**** → CHCH*** + CO*	-1.01	0.66	-0.16	0.04	-0.10	0.02

#	Facet	Surface reactions	Gas		Water		1,4-dioxane	
			ΔG_{Rxn} (eV)	ΔG_{TS} (eV)	$\Delta\Delta G_{Rxn}^{water}$ (eV)	$\Delta\Delta G_{TS}^{water}$ (eV)	$\Delta\Delta G_{Rxn}$ (eV)	$\Delta\Delta G_{TS}$ (eV)
19	100	CH_2CH*** → CHCH** + H *	-0.51	0.41	-0.14	-0.02	-0.09	-0.01
	111	CH_2CH*** + * → CHCH*** + H *	0.04	0.66	-0.03	-0.02	-0.01	-0.01
20	100	CH_2CH_2** + 2* → CH_2CH*** +H *	0.37	1.47	-0.21	0.01	-0.13	0.01
	111	CH_2CH_2** + 2* → CH_2CH*** + H *	0.30	1.06	-0.05	-0.01	-0.03	0.00
21	100	CH_2CH*** → CH_2C* + H* + *	0.01	0.62	-0.08	0.00	-0.06	-0.01
	111	CH_2CH*** → CH_2C** + H*	-0.29	0.52	-0.03	-0.02	-0.02	-0.01
22	100	CH_3C* + * → CH_2C* + H*	0.48	1.00	-0.18	-0.09	-0.13	-0.06
	111	CH_3C* + 2* → CH_2C** + H*	0.59	1.30	-0.05	-0.04	-0.03	-0.03
23	100	CH_3CH* + 3* → CH_2CH*** + H*	0.00	0.68	-0.31	-0.15	-0.20	-0.09
	111	CH_3CH** + 2* → CH_2CH*** + H*	-0.03	0.69	-0.08	-0.08	-0.04	-0.04
24	100	CH_3CH* + * → CH_3C* + H*	-0.47	0.28	-0.20	-0.09	-0.13	-0.07
	111	CH_3CH** → CH_3C* + H*	-0.91	0.17	-0.06	-0.03	-0.03	-0.01
25	100	CH_3CH_2* + * → CH_3CH* + H*	0.02	0.50	-0.16	-0.04	-0.10	-0.03
	111	CH_3CH_2* + 2* → CH_3CH** + H*	0.03	0.81	-0.04	-0.04	-0.01	0.00
26	100	CH_3CH_3* + * → CH_3CH_2* + H*	0.35	0.68	-0.17	-0.09	-0.09	-0.05
	111	CH_3CH_3* + * → CH_3CH_2* + H*	0.27	0.77	-0.02	-0.05	0.00	-0.01
27	100	CH_3CH_2* + 2* → CH_2CH_2** + H*	-0.34	0.33	-0.26	-0.09	-0.17	-0.06
	111	CH_3CH_2* + 2* → CH_2CH_2** + H*	-0.31	0.50	-0.07	-0.04	-0.03	0.00
28	100	CH_3CH_2COOH* + 2* → CH_3CH_2COO** + H*	-0.50	0.56	-0.15	0.01	-0.10	-0.01
	111	CH_3CH_2COOH* + 2* → CH_3CH_2COO** + H*	-0.11	0.47	0.02	-0.02	0.01	0.01
29	100	CH_3CH_2COO** → CH_3CH_2* + CO_2*	0.42	1.52	0.07	-0.03	0.11	-0.02
	111	CH_3CH_2COO** → CH_3CH_2* + CO_2*	0.16	1.41	0.05	-0.05	0.05	-0.02
30	100	CH_3CH_2COO** + 2* → CH_3CHCOO*** + H*	0.54	0.95	-0.23	-0.05	-0.11	0.02
	111	CH_3CH_2COO** + 2* → CH_3CHCOO*** + H*	0.91	1.31	-0.19	-0.15	-0.06	-0.04
31	100	$CH_3CHCOOH$** + 2* → CH_3CHCOO*** + H*	0.05	0.70	-0.20	0.01	-0.14	0.00
	111	$CH_3CHCOOH$** + 2* → CH_3CHCOO*** + H*	0.09	0.79	-0.16	-0.07	-0.07	-0.03
32	100	$CH_3CHCOOH$** + * → CH_3CH* + COOH**	0.44	1.36	-0.10	-0.03	-0.04	-0.02
	111	$CH_3CHCOOH$** + 2* → CH_3CH** + COOH*	-0.03	1.13	-0.11	-0.05	-0.04	-0.01
33	100	CH_3CHCOO*** → CH_3CH* + CO_2* + *	-0.10	1.44	0.14	0.06	0.12	0.04
	111	CH_3CHCOO*** → CH_3CH** + CO_2*	-0.73	0.69	0.19	0.01	0.10	-0.02
34	100	CH_3CHCOO*** → CH_3CCOO** + H*	0.39	1.03	-0.29	-0.13	-0.20	-0.07
	111	CH_3CHCOO*** + * → CH_3CCOO*** + H*	0.46	1.15	-0.15	-0.11	-0.10	-0.06
35	100	CH_3CCOOH** + * → CH_3CCOO** + H*	0.32	1.18	-0.31	-0.06	-0.21	0.00
	111	CH_3CCOOH*** + * → CH_3CCOO*** + H*	0.55	1.19	-0.20	-0.06	-0.09	0.01
36	100	CH_3CCOOH** + * → CH_3C* + COOH**	-0.15	1.49	-0.12	-0.02	-0.04	0.02
	111	CH_3CCOOH*** → CH_3C* + COOH**	-0.94	0.73	-0.07	-0.01	0.00	0.02
37	100	$CH_2CHCOOH$*** + 2* → CH_2CH*** + COOH**	0.88	1.37	-0.21	-0.02	-0.12	-0.02
	111	$CH_2CHCOOH$*** + 2* → CH_2CH*** + COOH**	0.69	1.91	-0.13	-0.05	-0.06	-0.02
38	100	CH_3CCOO** → CH_3C* + CO_2*	-0.96	1.88	0.23	0.19	0.19	0.12
	111	CH_3CCOO*** → CH_3C* + CO_2* + *	-2.10	0.20	0.28	0.24	0.17	0.14
39	100	COOH** → CO_2* + H*	-0.49	0.35	0.03	0.03	0.02	0.00
	111	COOH** → CO_2* + H*	-0.61	0.29	0.15	0.01	0.07	-0.01

#	Facet	Surface reactions	Gas		Water		1,4-dioxane	
			ΔG_{Rxn} (eV)	ΔG_{TS} (eV)	$\Delta\Delta G^{water}_{Rxn}$ (eV)	$\Delta\Delta G^{water}_{TS}$ (eV)	$\Delta\Delta G_{Rxn}$ (eV)	$\Delta\Delta G_{TS}$ (eV)
40	100	$COOH^{**} \rightarrow CO^{*} + OH^{*}$	-0.46	0.22	-0.10	-0.06	-0.07	-0.03
	111	$COOH^{**} \rightarrow CO^{*} + OH^{*}$	-0.28	0.61	-0.07	-0.02	-0.03	-0.01
41	100	$H_2O^{*} + {*} \rightarrow OH^{*} + H^{*}$	0.55	1.26	-0.13	-0.14	-0.10	-0.09
	111	$H_2O^{*} + {*} \rightarrow OH^{*} + H^{*}$	0.69	1.17	0.03	-0.05	0.03	-0.03
42	100	$CH_3CH_3(g) + {*} \rightarrow CH_3CH_3^{*}$	0.62	N/A	-0.08	N/A	-0.04	N/A
	111	$CH_3CH_3(g) + {*} \rightarrow CH_3CH_3^{*}$	0.63	N/A	-0.03	N/A	-0.03	N/A
43	100	$CH_2CH_2(g) + 2{*} \rightarrow CH_2CH_2^{**}$	-0.15	N/A	-0.19	N/A	-0.09	N/A
	111	$CH_2CH_2(g) + 2{*} \rightarrow CH_2CH_2^{**}$	0.03	N/A	-0.09	N/A	-0.03	N/A
44	100	$H_2O(g) + {*} \rightarrow H_2O^{*}$	0.31	N/A	-0.18	N/A	-0.08	N/A
	111	$H_2O(g) + {*} \rightarrow H_2O^{*}$ (water: solvent in liquid phase env)	0.38	N/A	-0.11	N/A	-0.05	N/A
45	100	$CO_2(g) + {*} \rightarrow CO_2^{*}$	0.42	N/A	-0.11	N/A	-0.03	N/A
	111	$CO_2(g) + {*} \rightarrow CO_2^{*}$	0.49	N/A	-0.07	N/A	-0.05	N/A
46	100	$CHCH(g) + 2{*} \rightarrow CHCH^{**}$	-1.73	N/A	-0.22	N/A	-0.11	N/A
	111	$CHCH(g) + 3{*} \rightarrow CHCH^{***}$	-0.86	N/A	-0.13	N/A	-0.04	N/A
47	100	$CO(g) + {*} \rightarrow CO^{*}$	-0.42	N/A	-0.25	N/A	-0.15	N/A
	111	$CO(g) + {*} \rightarrow CO^{*}$	-0.46	N/A	-0.24	N/A	-0.15	N/A
48	100	$H_2(g) + 2{*} \rightarrow H^{*} + H^{*}$	-0.04	N/A	-0.32	N/A	-0.21	N/A
	111	$H_2(g) + 2{*} \rightarrow H^{*} + H^{*}$	-0.25	N/A	-0.04	N/A	-0.02	N/A
49	100	$C_4H_8O_2(g) + {*} \rightarrow C_4H_8O_2^{*}$	0.10	N/A	-0.31	N/A	-0.16	N/A
	111	$C_4H_8O_2(g) + {*} \rightarrow C_4H_8O_2^{*}$ (1,4-dioxane: solvent in liquid phase env)	0.46	N/A	-0.23	N/A	-0.14	N/A

Table 2. TOFs (s^{-1}) and surface coverage of the most abundant surface intermediates in vapor phase on Pd(100) and Pd(111) at 473 K, a propanoic acid fugacity of 1 bar, a CO fugacity of 1×10^{-5}, 1×10^{-3}, 1×10^{-1} bar, and an H_2 fugacity of 0.01, 1, and 10 bar.

P_{H_2} (Bar)	Facet	P_{CO}= 1×10^{-5} bar				P_{CO}= 1×10^{-3} bar				P_{CO}= 1×10^{-1} bar			
		TOF (s^{-1})	θ_{CO}	θ_H	θ^*	TOF (s^{-1})	θ_{CO}	θ_H	θ^*	TOF (s^{-1})	θ_{CO}	θ_H	θ^*
0.01	100	2.45×10^{-2}	0.19	0.12	0.64	9.11×10^{-4}	0.28	0.06	0.65	2.98×10^{-5}	0.39	0.02	0.57
	111	2.57×10^{-9}	0.21	0.55	0.24	7.17×10^{-8}	0.74	0.05	0.16	1.14×10^{-10}	0.93	0.01	0.02
1	100	1.17×10^{-3}	0.19	0.25	0.55	2.45×10^{-5}	0.29	0.16	0.55	2.91×10^{-6}	0.39	0.08	0.51
	111	1.77×10^{-13}	0.01	0.95	0.04	1.02×10^{-10}	0.44	0.48	0.08	2.19×10^{-11}	0.92	0.02	0.02
10	100	2.80×10^{-4}	0.19	0.33	0.47	5.87×10^{-6}	0.29	0.23	0.47	7.76×10^{-7}	0.40	0.14	0.45
	111	5.27×10^{-15}	0.01	0.98	0.01	4.91×10^{-14}	0.20	0.78	0.02	2.14×10^{-11}	0.89	0.07	0.02

Table 3. TOFs (s^{-1}) and surface coverage of the most abundant surface intermediates in vapor phase on Pd(100) and Pd(111) at a propanoic acid fugacity of 1 bar, CO fugacity of 1×10^{-5} bar, and an H_2 fugacity of 0.01 bar in a temperature range from 473 to 523 K.

Temperature (K)	Pd(100)					Pd(111)			
	TOF (s^{-1})	θ_{CO}	θ_H	θ^*	θ_{CHCH}	TOF (s^{-1})	θ_{CO}	θ_H	θ^*
473	2.45×10^{-2}	0.19	0.12	0.64	0.04	2.57×10^{-9}	0.21	0.55	0.24
498	7.48×10^{-2}	0.16	0.10	0.56	0.16	1.47×10^{-8}	0.13	0.54	0.31
523	1.01×10^{-1}	0.13	0.09	0.42	0.32	1.11×10^{-7}	0.08	0.54	0.38

Table 4. Product selectivity via DCN and DCX pathways under vapor and liquid phase reaction conditions at a temperature of 473 K, a propanoic acid fugacity of 1 bar, a CO fugacity of 1×10^{-5} bar, and a hydrogen fugacity of 0.01 bar over Pd(100) and Pd(111). Solvation calculation results for water and 1,4-dioxane are also shown with ±10% of the default COSMO Pd cavity radius.

Facet	Routes	gas	water (default)	water (+10%)	water (-10%)	1, 4-dioxane (default)	1, 4-dioxane (+10%)	1, 4-dioxane (-10%)
Pd(100)	S_{DCN}	1.00	0.97	0.94	0.93	0.99	0.99	0.96
	S_{DCX}	0.00	0.03	0.06	0.07	0.01	0.01	0.04
Pd(111)	S_{DCN}	0.72	0.01	0.01	0.01	0.79	0.67	0.23
	S_{DCX}	0.28	0.99	0.99	0.99	0.21	0.33	0.77

Table 5. TOFs (s^{-1}) and surface coverage of the most abundant surface intermediates in liquid water on Pd(100) and Pd(111) at 473 K, a propanoic acid fugacity of 1 bar, a CO fugacity of 1×10^{-5}, 1×10^{-3}, 1×10^{-1} bar, and an H_2 fugacity of 0.01, 1, and 10 bar. Only absolute surface coverage (θ) values larger 0.01 are shown.

P_{H_2} (Bar)	P_{CO} (Bar)	Facet	TOF (s^{-1})	θ_{CO}	θ_H	θ^*	θ_{PAc}
0.01	10^{-5}	100	1.35×10^{-3}	0.32	0.17	0.38	-
		111	1.30×10^{-8}	0.70	0.01	0.23	0.04
	10^{-3}	100	2.15×10^{-5}	0.37	0.06	0.54	-
		111	9.21×10^{-11}	0.84	0.01	0.10	0.05
	10^{-1}	100	1.20×10^{-6}	0.43	0.01	0.54	-
		111	2.87×10^{-13}	0.96	-	0.02	0.02
1	10^{-5}	100	1.46×10^{-4}	0.29	0.30	0.39	-
		111	1.63×10^{-9}	0.63	0.19	0.17	-
	10^{-3}	100	8.62×10^{-7}	0.36	0.16	0.47	-
		111	9.26×10^{-12}	0.84	-	0.10	0.05
	10^{-1}	100	9.28×10^{-8}	0.44	0.05	0.50	-
		111	2.87×10^{-14}	0.96	-	0.02	0.02
10	10^{-5}	100	6.36×10^{-5}	0.29	0.37	0.33	-
		111	1.37×10^{-11}	0.33	0.65	0.02	-
	10^{-3}	100	1.80×10^{-7}	0.36	0.22	0.41	-
		111	2.98×10^{-12}	0.84	0.01	0.10	0.04
	10^{-1}	100	1.92×10^{-8}	0.44	0.10	0.45	-
		111	9.05×10^{-15}	0.95	-	0.02	0.02

Table 6. TOFs (s^{-1}) and surface coverage of the most abundant surface intermediates in liquid water and liquid 1,4-dioxane on Pd(100) and Pd(111) at a propanoic acid fugacity of 1 bar, CO fugacity of 1×10^{-5} bar, and an H_2 fugacity of 0.01 bar in a temperature range from 473 to 523 K. Only absolute surface coverage (θ) values larger 0.01 are shown.

	T (K)	Facet	TOF (s^{-1})	θ_{CO}	θ_{H}	θ^{*}	$\theta_{CH_2CHCOOH}$	$\theta_{CH_3CH_2COO}$	θ_{CHCH}	θ_{CH_3C}	θ_{PAc}
Water	473	100	1.35×10^{-3}	0.32	0.17	0.38	0.05	0.07	0.01	-	-
		111	1.30×10^{-8}	0.70	0.01	0.23	-	-	-	-	0.04
	498	100	2.01×10^{-2}	0.32	0.17	0.21	0.07	0.06	0.14	0.01	-
		111	2.77×10^{-7}	0.65	0.02	0.11	-	-	-	0.20	0.01
	523	100	4.94×10^{-2}	0.29	0.16	0.10	0.01	0.02	0.38	0.03	-
		111	1.36×10^{-6}	0.56	0.01	0.04	-	-	-	0.37	-
1,4 -Dioxane	473	100	7.15×10^{-4}	0.24	0.13	0.62	-	0.01	-	-	-
		111	1.44×10^{-7}	0.63	0.06	0.09	-	-	-	0.19	0.01
	498	100	1.48×10^{-2}	0.22	0.13	0.55	-	0.01	0.06	-	-
		111	1.69×10^{-6}	0.54	0.09	0.14	-	-	-	0.22	-
	523	100	4.73×10^{-2}	0.20	0.14	0.40	-	-	0.25	-	-
		111	1.74×10^{-5}	0.46	0.14	0.25	-	-	-	0.14	-

Table 7. TOFs (s^{-1}) and surface coverage of the most abundant surface intermediates (CO and H) and others in 1,4-dioxane on Pd(100) and Pd(111) at 473 K, a propanoic acid fugacity of 1 bar, a CO fugacity of 1×10^{-5}, 1×10^{-3}, 1×10^{-1} bar, and an H_2 fugacity of 0.01, 1, and 10 bar. Only absolute surface coverage (θ) values larger 0.01 are shown.

P_{H_2} (Bar)	P_{CO} (Bar)	Facet	TOF (s^{-1})	θ_{CO}	θ_H	θ^*	θ_{PAc}	θ_{CH_3C}
0.01	10^{-5}	100	7.15×10^{-4}	0.24	0.13	0.62	-	-
		111	1.44×10^{-7}	0.63	0.06	0.09	-	0.19
	10^{-3}	100	9.12×10^{-5}	0.36	0.07	0.52	-	-
		111	1.14×10^{-8}	0.85	-	0.01	0.12	-
	10^{-1}	100	2.45×10^{-5}	0.48	0.03	0.35	-	-
		111	2.84×10^{-12}	0.95	-	-	0.04	-
1	10^{-5}	100	1.61×10^{-6}	0.21	0.22	0.56	-	-
		111	2.32×10^{-11}	0.22	0.73	0.05	-	-
	10^{-3}	100	7.53×10^{-7}	0.34	0.16	0.49	-	-
		111	1.59×10^{-10}	0.84	0.03	0.02	0.09	-
	10^{-1}	100	1.19×10^{-6}	0.46	0.11	0.37	-	-
		111	2.85×10^{-13}	0.95	-	-	0.04	-
10	10^{-5}	100	1.55×10^{-7}	0.20	0.27	0.52	-	-
		111	1.51×10^{-13}	0.08	0.91	0.01	-	-
	10^{-3}	100	6.99×10^{-8}	0.33	0.21	0.45	-	-
		111	1.10×10^{-10}	0.79	0.16	0.02	0.03	-
	10^{-1}	100	1.39×10^{-7}	0.45	0.15	0.37	-	-
		111	9.14×10^{-14}	0.95	-	-	0.04	-

Table 8. Degree of rate control for various steps over Pd(100) and Pd(111) under gas and liquid phase reaction conditions, including ±10% of the default COSMO palladium cavity radius in liquid water and 1,4-dioxane, at a temperature of 473 K, a propanoic acid fugacity of 1 bar, a CO fugacity of 1×10^{-5} bar, and a hydrogen fugacity of 0.01 bar.

Facet	Reaction step no.	gas	water (default)	water (+10%)	water (-10%)	1,4-dioxane (default)	1,4-dioxane (+10%)	1,4-dioxane (-10%)
Pd(100)	01	0.00	0.01	0.04	0.00	0.01	0.02	0.00
	02	0.18	0.02	0.01	0.07	0.07	0.05	0.14
	11	0.47	0.66	0.58	0.51	0.81	0.83	0.68
	21	0.16	0.04	0.02	0.13	0.02	-0.01	0.03
	25	0.13	0.01	0.01	0.02	0.01	0.00	0.01
	29	0.01	0.03	0.06	0.08	0.01	0.01	0.05
Pd(111)	01	0.71	0.01	0.01	0.01	0.14	0.19	0.00
	02	0.00	0.00	0.00	0.00	0.00	0.00	0.00
	11	0.01	0.00	-0.01	-0.01	0.00	0.00	0.00
	21	0.00	0.00	0.01	0.01	0.00	0.00	0.00
	25	-0.01	0.00	0.00	0.00	0.97	0.98	0.20
	29	0.28	0.98	0.98	0.99	-0.22	-0.32	0.77

Table 9. Degrees of thermodynamic rate control for H* and CO* (the most abundant surface species) under gas and liquid phase reaction conditions at a temperature of 473 K, a propanoic acid fugacity of 1 bar, a CO fugacity of 1×10^{-5} bar, and a hydrogen fugacity of 0.01 bar over Pd(100) and Pd(111). Results from solvation calculations with ±10% of the default COSMO Pd cavity are also shown for liquid water and 1,4-dioxane.

Facet	Surface species	gas	water (default)	water (+10%)	water (10%)	1,4-dioxane (default)	1,4-dioxane (+10%)	1,4-dioxane (-10%)
Pd(100)	H*	-1.14	-4.10	-3.56	-1.49	-1.33	-1.36	-1.40
	CO*	-1.55	-3.23	-2.30	-1.89	-1.82	-2.13	-0.91
Pd(111)	H*	-3.49	-1.17	-1.25	-1.11	-1.44	-1.42	-1.26
	CO*	1.98	-0.82	-0.80	-0.89	-0.85	-0.71	-0.95

Table 10. Degree of selectivity control (DSC) for reaction steps that have impact on the DCN and DCX pathway under gas and liquid phase reaction conditions at a temperature of 473 K, a propanoic acid fugacity of 1 bar, a CO fugacity of 1×10^{-5} bar, and a hydrogen fugacity of 0.01 bar over Pd(100) and Pd(111). Results from solvation calculations with ±10% of the default COMSOL Pd cavity are also shown for liquid water and 1,4-dioxane. Only absolute DSC values larger 0.01 are shown.

Reaction Steps	Facet	Path	gas	water (default)	water (+10%)	water (-10%)	1, 4-dioxane (default)	1, 4-dioxane (+10%)	1, 4-dioxane (-10%)
Step-1	100	DSC_{DCN}	-	-	-	-	-	-	-
		DSC_{DCX}	-	-0.02	-0.04	-	-0.01	-0.02	-
	111	DSC_{DCN}	0.29	0.01	0.02	-	0.03	0.05	-0.03
		DSC_{DCX}	-0.71	0.00	-	-	-0.12	-0.09	0.01
Step-2	100	DSC_{DCN}	-	-	-	0.01	-	-	-
		DSC_{DCX}	-0.03	-0.03	-0.01	-0.11	-0.01	-0.05	-0.14
	111	DSC_{DCN}	-	-	-	-	-	-	-
		DSC_{DCX}	-	-	-	-	-	-	-
Step-11	100	DSC_{DCN}	-	0.02	0.03	0.04	0.01	0.01	0.03
		DSC_{DCX}	-0.92	-0.68	0.59	-0.57	-0.83	-0.84	-0.70
	111	DSC_{DCN}	-	-	-	-	-	-	-
		DSC_{DCX}	-	-	-	-	-	-	-
Step-21	100	DSC_{DCN}	-	-	-	-	-	-	-
		DSC_{DCX}	0.03	-0.02	-0.01	-0.06	-0.01	-	-0.02
	111	DSC_{DCN}	-	-	-	-	-	-	-
		DSC_{DCX}	-	-	-	-	-	-	-
Step-25	100	DSC_{DCN}	-	-	-	-	-	-	-
		DSC_{DCX}	0.02	-0.01	-	0.01	-	-	-
	111	DSC_{DCN}	-	-	-	-	0.09	0.17	0.07
		DSC_{DCX}	-	-	-	-	-0.35	-0.35	-0.02
Step-29	100	DSC_{DCN}	-	-0.03	-0.06	-0.07	-0.01	-0.01	-0.04
		DSC_{DCX}	0.08	0.96	0.93	0.88	0.95	0.97	0.95
	111	DSC_{DCN}	-0.29	-0.98	-0.98	-0.99	-0.22	-0.33	-0.77
		DSC_{DCX}	0.71	0.02	0.02	0.01	0.79	0.67	0.23

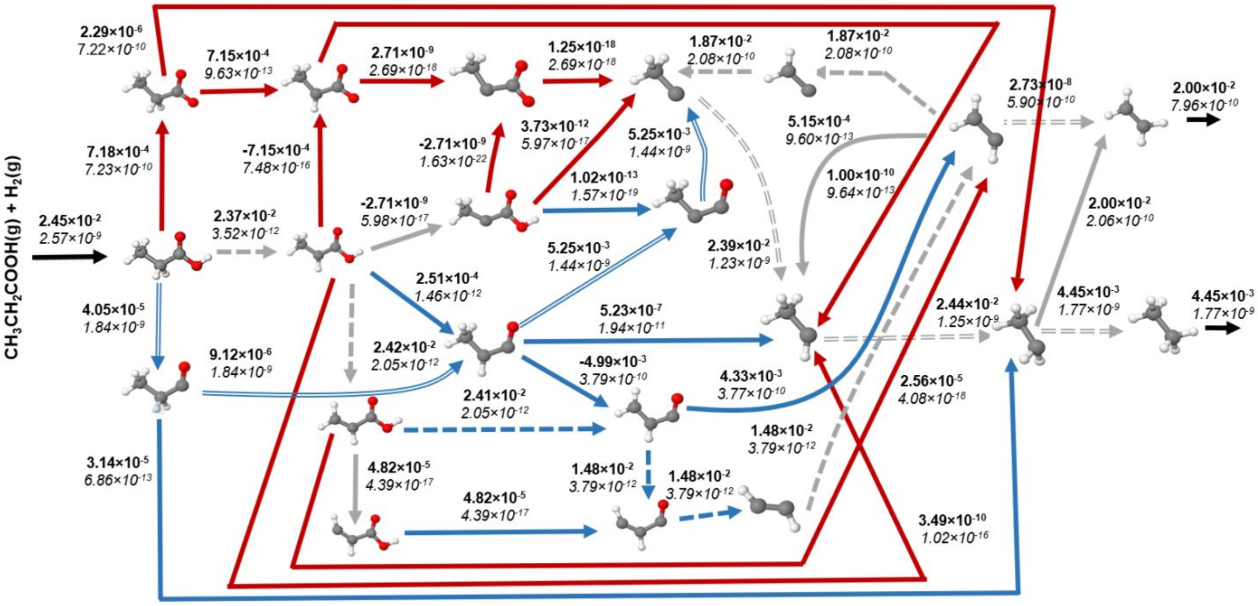

Figure 1. TOFs (s^{-1}) of various elementary steps at a temperature of 473 K and vapor phase reaction conditions of a propanoic acid partial pressure of 1 bar, a CO partial pressure of 1×10^{-5} bar, and a hydrogen partial pressure of 0.01 bar. Black arrows symbolize adsorption/desorption steps, blue arrows are DCN steps, red arrows are DCX steps, and gray arrows are the steps involved in both DCN and DCX steps. Bold numbers indicate the rate of elementary steps on Pd(100), while italic numbers indicate the rate on Pd(111). Dominate pathways over Pd(100) and Pd(111) are shown in dashed arrows and double line arrows, respectively. Gray double and dashed line arrows demonstrate overlapping dominant pathways on Pd(100) and Pd(111).

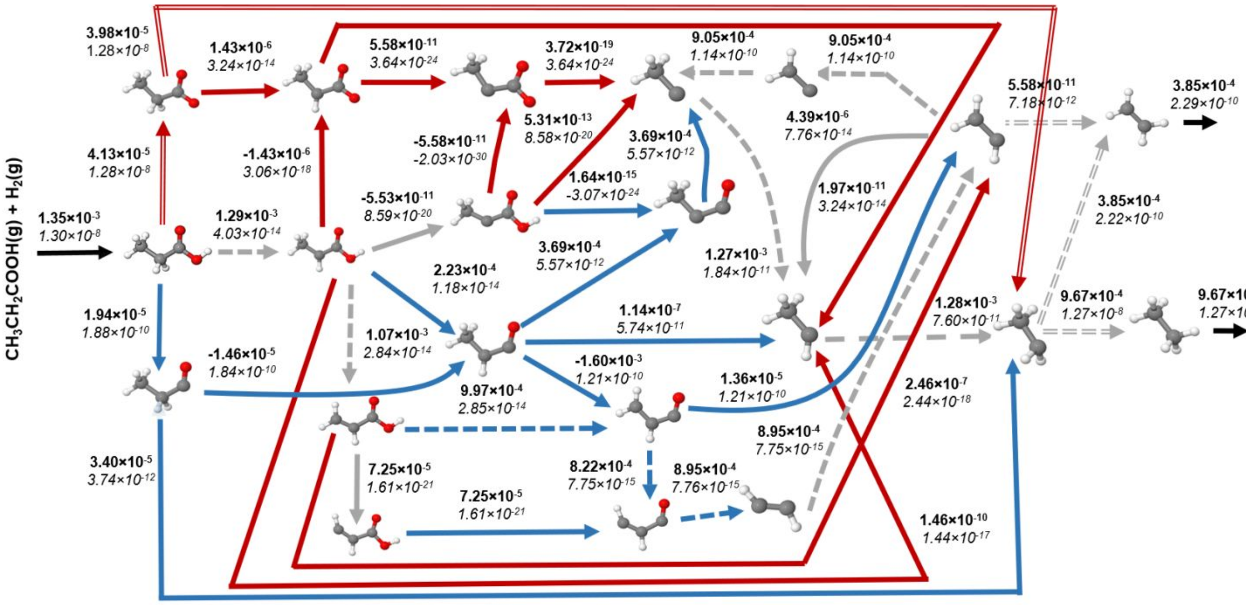

Figure 2. TOFs (s^{-1}) of various elementary steps at a temperature of 473 K and liquid water reaction conditions with default palladium COSMO cavity radius, a propanoic acid fugacity of 1 bar, a CO fugacity of 1×10^{-5} bar, and a hydrogen fugacity of 0.01 bar. Black arrows symbolize adsorption/desorption steps, blue arrows are DCN steps, red arrows are DCX steps, and gray arrows are the steps involved in both DCN and DCX steps. Bold numbers indicate the rate of elementary steps on Pd(100), while italic numbers indicate the rate on Pd(111). Dominate pathways over Pd(100) and Pd(111) are shown in dashed arrows and double line arrows, respectively. Gray double and dashed line arrows demonstrate overlapping dominant pathways for Pd(100) and Pd(111).

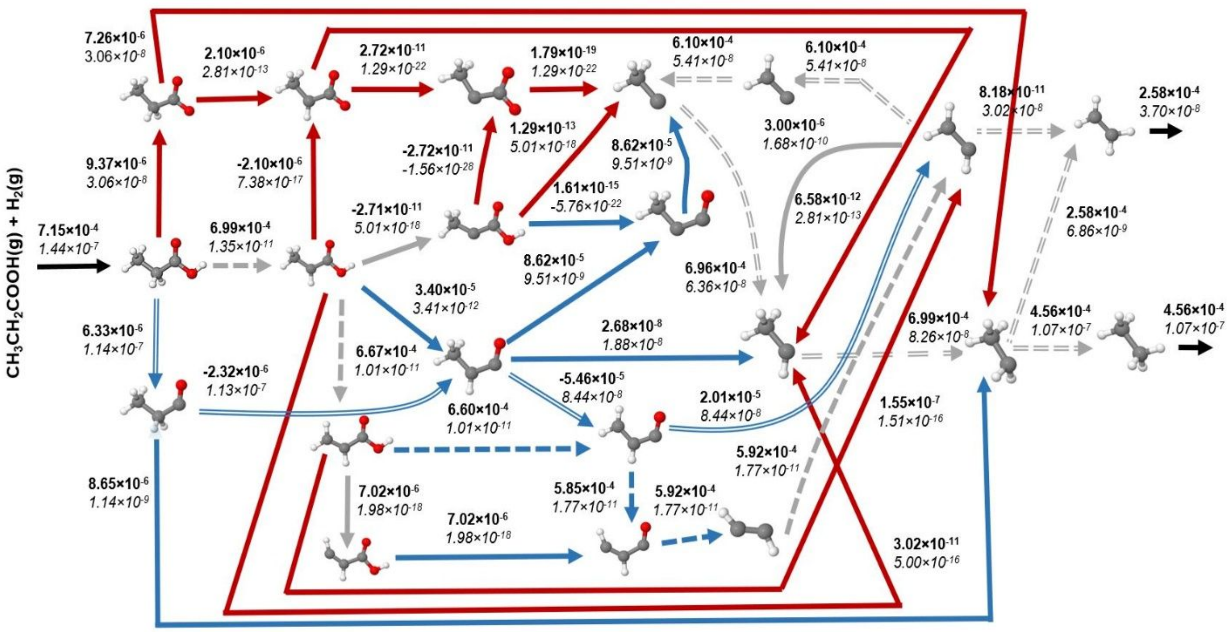

Figure 3. TOFs (s^{-1}) of various elementary steps at a temperature of 473 K and liquid 1,4-dioxane reaction conditions with default palladium COSMO cavity radius, a propanoic acid fugacity of 1 bar, a CO fugacity of 1×10^{-5} bar, and a hydrogen fugacity of 0.01 bar. Black arrows symbolize adsorption/desorption steps, blue arrows are DCN steps, red arrows are DCX steps, and gray arrows are the steps involved in both DCN and DCX steps. Bold numbers indicate the rate of elementary steps on Pd(100), while italic numbers indicate the rate on Pd(111). Dominate pathways over Pd(100) and Pd(111) are shown in dashed arrows and double line arrows, respectively. Gray double and dashed line arrows demonstrate overlapping dominant pathways for Pd(100) and Pd(111).

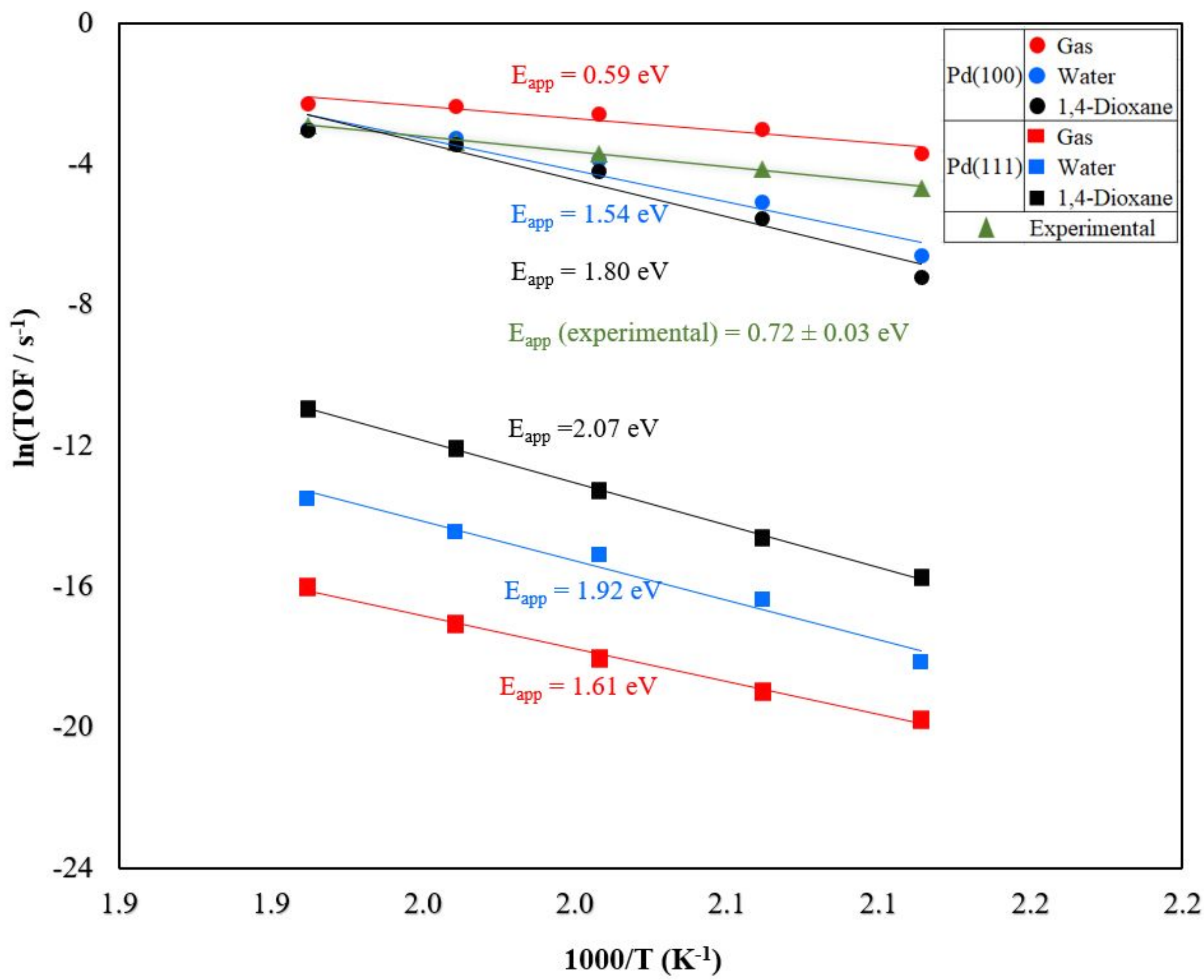

Figure 4. Arrhenius plot for the HDO of propanoic acid in various reaction media, a reaction temperature between 473 and 523 K, a propanoic acid fugacity of 1 bar, a CO fugacity of 1×10^{-5} bar, and a hydrogen fugacity of 0.01 bar over Pd(100) and Pd(111). Experimental values obtained from Lugo-José et al.[19] under gas phase reaction conditions are indicated by triangular markers.

(a)

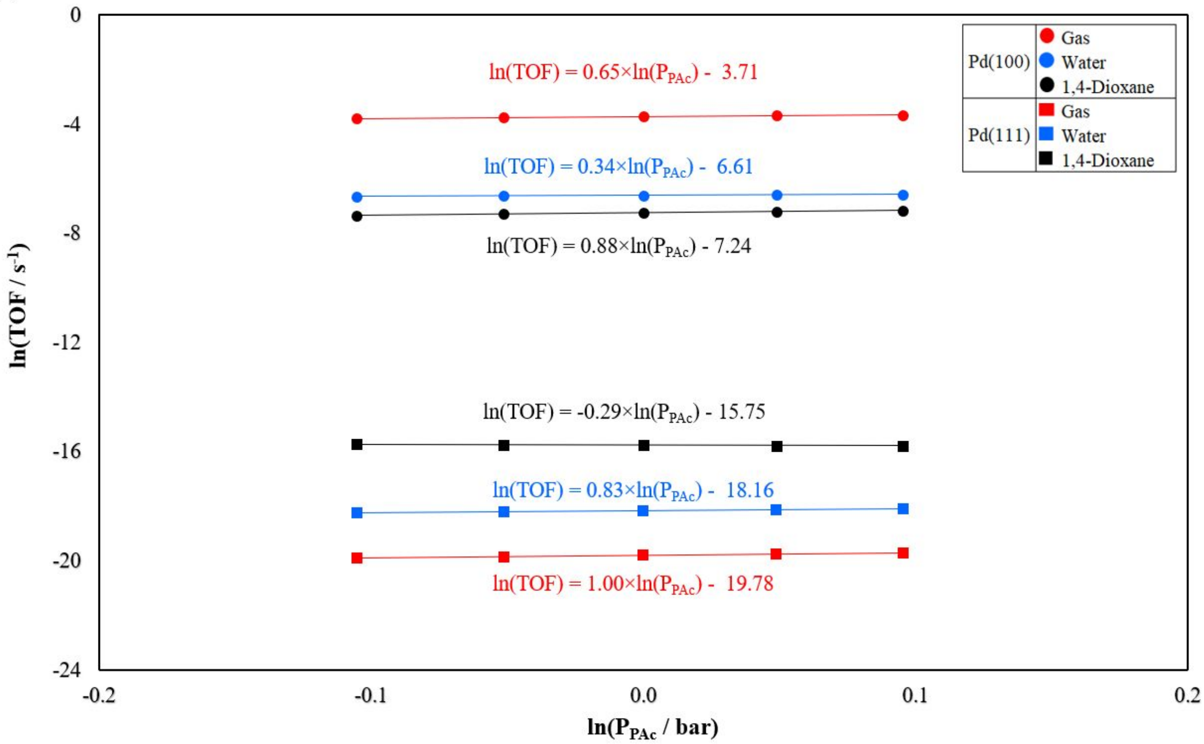
ln(TOF) = 0.65×ln(P_PAc) - 3.71
ln(TOF) = 0.34×ln(P_PAc) - 6.61
ln(TOF) = 0.88×ln(P_PAc) - 7.24
ln(TOF) = -0.29×ln(P_PAc) - 15.75
ln(TOF) = 0.83×ln(P_PAc) - 18.16
ln(TOF) = 1.00×ln(P_PAc) - 19.78
Pd(100) Gas Water 1,4-Dioxane
Pd(111) Gas Water 1,4-Dioxane
ln(TOF / s-1)
ln(P_PAc / bar)

(b)

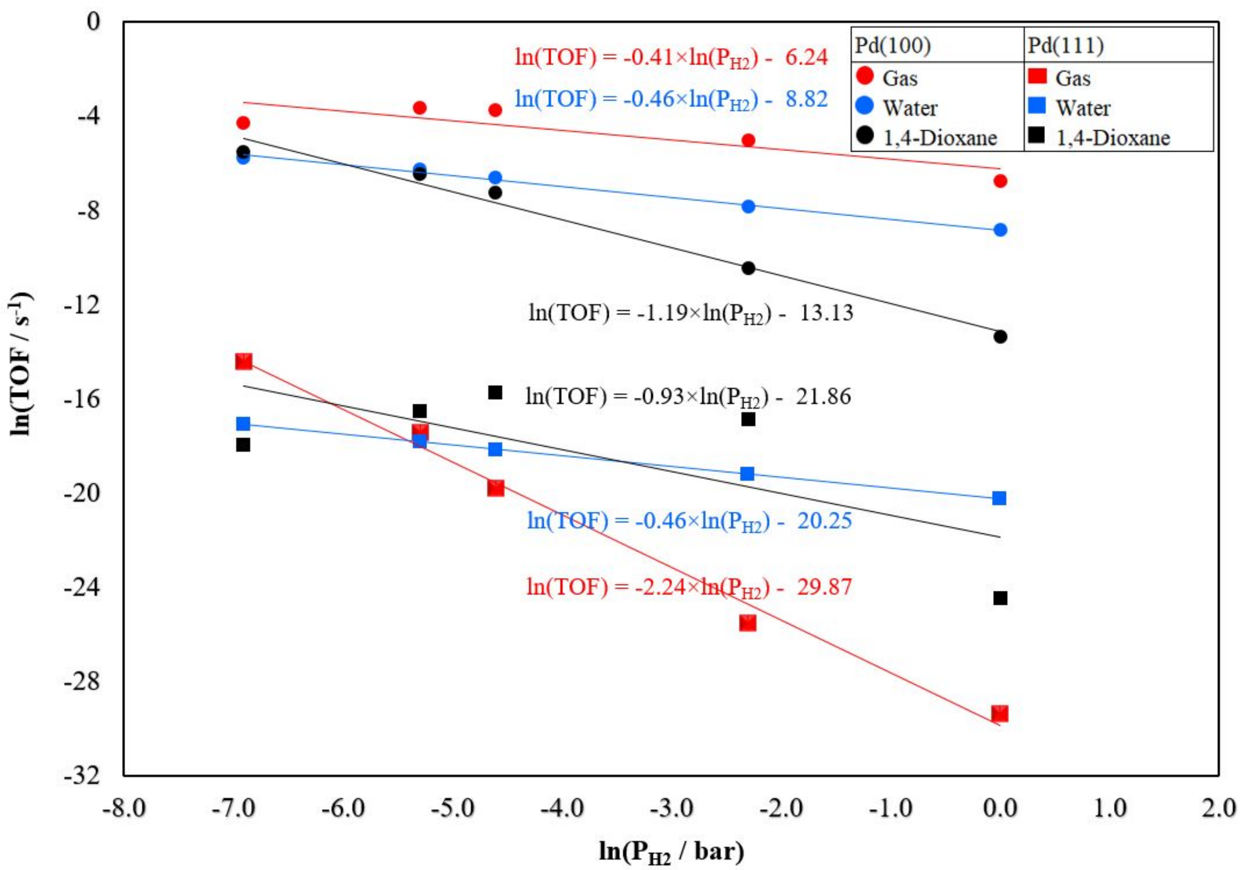
ln(TOF) = -0.41×ln(P_H2) - 6.24
ln(TOF) = -0.46×ln(P_H2) - 8.82
ln(TOF) = -1.19×ln(P_H2) - 13.13
ln(TOF) = -0.93×ln(P_H2) - 21.86
ln(TOF) = -0.46×ln(P_H2) - 20.25
ln(TOF) = -2.24×ln(P_H2) - 29.87
Pd(100) Gas Water 1,4-Dioxane
Pd(111) Gas Water 1,4-Dioxane
ln(TOF / s-1)
ln(P_H2 / bar)

(c)

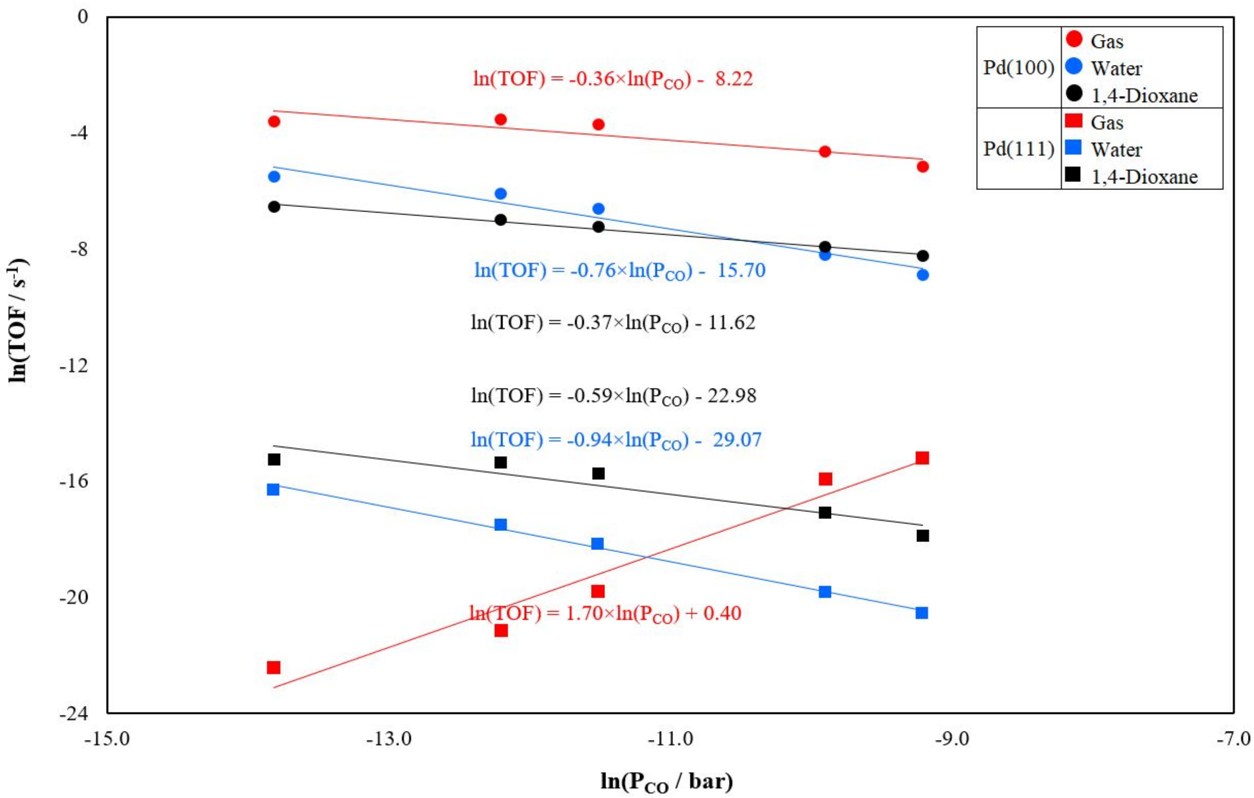

Figure 5. Reaction orders in various reaction media of (a) propanoic acid (b) H_2, and (c) CO at a temperature of 473 K, a propanoic acid fugacity of 1 bar, a hydrogen fugacity of 0.01 bar, and a CO fugacity of 1×10^{-5} bar for Pd(100) and Pd(111).

References:

1. S. Behtash, J. Lu, C. T. Williams, J. R. Monnier and A. Heyden, *J. Phys. Chem. C*, 2015, **119**, 1928–1942.
2. J. C. Serrano-Ruiz and J. A. Dumesic, *Energy Environ. Sci.*, 2010, **4**, 83–99.
3. L. Nykänen, J. Andersin and K. Honkala, *Phys. Rev. B*, 2010, **81**, 075417.
4. G. Knothe, *Fuel Processing Technology*, 2005, **86**, 1059–1070.
5. M. J. Ramos, C. M. Fernández, A. Casas, L. Rodríguez and A. Pérez, *Bioresour. Technol.*, 2009, **100**, 261–268.
6. D. L. Klass, in *Encyclopedia of Energy*, Elsevier, 2004, pp. 193–212.
7. G. W. Huber, P. O'Connor and A. Corma, *Applied Catalysis A: General*, 2007, **329**, 120–129.
8. D. Kubička, P. Šimáček and N. Žilková, *Top Catal*, 2009, **52**, 161–168.
9. D. C. Elliott, D. Beckman, A. V. Bridgwater, J. P. Diebold, S. B. Gevert and Y. Solantausta, *Energy Fuels*, 1991, **5**, 399–410.
10. D. Mohan, C. U. Pittman and P. H. Steele, *Energy Fuels*, 2006, **20**, 848–889.
11. P. Mäki-Arvela, I. Kubickova, M. Snåre, K. Eränen and D. Yu. Murzin, *Energy Fuels*, 2007, **21**, 30–41.
12. P. Mäki-Arvela, M. Snåre, K. Eränen, J. Myllyoja and D. Yu. Murzin, *Fuel*, 2008, **87**, 3543–3549.
13. I. L. Simakova, O. A. Simakova, A. V. Romanenko and D. Yu. Murzin, *Ind. Eng. Chem. Res.*, 2008, **47**, 7219–7225.
14. S. Lestari, P. Mäki-Arvela, J. Beltramini, G. Q. M. Lu and D. Y. Murzin, *ChemSusChem*, 2009, **2**, 1109–1119.
15. I. Simakova, O. Simakova, P. Mäki-Arvela, A. Simakov, M. Estrada and D. Yu. Murzin, *Applied Catalysis A: General*, 2009, **355**, 100–108.
16. W. F. Maier, W. Roth, I. Thies and P. V. R. Schleyer, *Chemische Berichte*, 1982, **115**, 808–812.
17. S. Lestari, P. Mäki-Arvela, I. Simakova, J. Beltramini, G. Q. M. Lu and D. Yu. Murzin, *Catal Lett*, 2009, **130**, 48–51.
18. L. Boda, G. Onyestyák, H. Solt, F. Lónyi, J. Valyon and A. Thernesz, *Applied Catalysis A, General*, 2010, **374**, 158–169.
19. Y. K. Lugo-José, J. R. Monnier and C. T. Williams, *Applied Catalysis A: General*, 2014, **469**, 410–418.
20. J. H. Sinfelt, *AIChE Journal*, 1973, **19**, 673–683.
21. G. A. Somorjai and J. Y. Park, *Angewandte Chemie International Edition*, 2008, **47**, 9212–9228.
22. G. C. Bond, *Surface Science*, 1985, **156**, 966–981.
23. C. R. Henry, C. Chapon, S. Giorgio and C. Goyhenex, in *Chemisorption and Reactivity on Supported Clusters and Thin Films: Towards an Understanding of Microscopic Processes in Catalysis*, eds. R. M. Lambert and G. Pacchioni, Springer Netherlands, Dordrecht, 1997, pp. 117–152.
24. P. E. Strizhak, *Theor Exp Chem*, 2013, **49**, 2–21.
25. C. P. Vinod, *Catalysis Today*, 2010, **154**, 113–117.
26. B. R. Cuenya, *Thin Solid Films*, 2010, **518**, 3127–3150.

27. F. Zaera, *Progress In Surface Science*, 2001, **69**, 1–98.
28. J. M. Martínez de la Hoz and P. B. Balbuena, *J. Phys. Chem. C*, 2011, **115**, 21324–21333.
29. B. Hammer and J. K. Nørskov, in *Advances in Catalysis*, Academic Press, 2000, vol. 45, pp. 71–129.
30. J. K. Nørskov, T. Bligaard, A. Logadottir, S. Bahn, L. B. Hansen, M. Bollinger, H. Bengaard, B. Hammer, Z. Sljivancanin, M. Mavrikakis, Y. Xu, S. Dahl and C. J. H. Jacobsen, *Journal of Catalysis*, 2002, **209**, 275–278.
31. M. Boudart, *Chem. Rev.*, 1995, **95**, 661–666.
32. B. Hammer, Y. Morikawa and J. K. Nørskov, *Phys. Rev. Lett.*, 1996, **76**, 2141–2144.
33. B. Hammer, O. H. Nielsen and J. K. Nrskov, *Catalysis Letters*, 1997, **46**, 31–35.
34. J. B. Butt and C. L. M. Joyal, *J. Chem. Soc., Faraday Trans.*, 1990, **86**, 2911–2917.
35. N. Marín-Astorga, G. Pecchi, J. L. G. Fierro and P. Reyes, *Catalysis Letters*, 2003, **91**, 115–121.
36. A. Borodziński, *Catalysis Letters*, 2001, **71**, 169–175.
37. A. Binder, M. Seipenbusch, M. Muhler and G. Kasper, *Journal of Catalysis*, 2009, **268**, 150–155.
38. R. Van Hardeveld and F. Hartog, *Surface Science*, 1969, **15**, 189–230.
39. Y. K. Lugo-José, J. R. Monnier, A. Heyden and C. T. Williams, *Catalysis Science & Technology*, 2014, **4**, 3909–3916.
40. S. Behtash, J. Lu, O. Mamun, C. T. Williams, J. R. Monnier and A. Heyden, *J. Phys. Chem. C*, 2016, **120**, 2724–2736.
41. S. Behtash, J. Lu, C. T. Williams, J. R. Monnier and A. Heyden, *J. Phys. Chem. C*, 2015, **119**, 1928–1942.
42. J. Lu, S. Behtash and A. Heyden, *J. Phys. Chem. C*, 2012, **116**, 14328–14341.
43. J. Lu, S. Behtash, M. Faheem and A. Heyden, *Journal of Catalysis*, 2013, **305**, 56–66.
44. S. Behtash, J. Lu, M. Faheem and A. Heyden, *Green Chem.*, 2014, **16**, 605–616.
45. S. Behtash, J. Lu and A. Heyden, *Catal. Sci. Technol.*, 2014, **4**, 3981–3992.
46. K. Abdelfatah, W. Yang, R. Vijay Solomon, B. Rajbanshi, A. Chowdhury, M. Zare, S. K. Kundu, A. Yonge, A. Heyden and G. Terejanu, *J. Phys. Chem. C*, 2019, **123**, 29804–29810.
47. I. Simakova, O. Simakova, P. Mäki-Arvela and D. Yu. Murzin, *Catalysis Today*, 2010, **150**, 28–31.
48. I. Simakova, B. Rozmysłowicz, O. Simakova, P. Mäki-Arvela, A. Simakov and D. Yu. Murzin, *Top Catal*, 2011, **54**, 460–466.
49. J. G. Immer, M. J. Kelly and H. H. Lamb, *Applied Catalysis A: General*, 2010, **375**, 134–139.
50. S. Lestari, P. Mäki-Arvela, K. Eränen, J. Beltramini, G. Q. Max Lu and D. Yu. Murzin, *Catal Lett*, 2010, **134**, 250–257.
51. M. Arend, T. Nonnen, W. F. Hoelderich, J. Fischer and J. Groos, *Applied Catalysis A: General*, 2011, **399**, 198–204.
52. G. Kresse and J. Hafner, *Phys. Rev. B*, 1993, **47**, 558–561.
53. G. Kresse and J. Furthmüller, *Computational Materials Science*, 1996, **6**, 15–50.
54. G. Kresse and D. Joubert, *Phys. Rev. B*, 1999, **59**, 1758–1775.
55. J. P. Perdew and Y. Wang, *Phys. Rev. B*, 1992, **45**, 13244–13249.

56. J. P. Perdew and W. Yue, *Phys. Rev. B*, 1986, **33**, 8800–8802.
57. H. J. Monkhorst and J. D. Pack, *Phys. Rev. B*, 1976, **13**, 5188–5192.
58. M. Methfessel and A. T. Paxton, *Phys. Rev. B*, 1989, **40**, 3616–3621.
59. G. Henkelman, B. P. Uberuaga and H. Jónsson, *J. Chem. Phys.*, 2000, **113**, 9901–9904.
60. G. Henkelman and H. Jónsson, *J. Chem. Phys.*, 1999, **111**, 7010–7022.
61. R. A. Olsen, G. J. Kroes, G. Henkelman, A. Arnaldsson and H. Jónsson, *J. Chem. Phys.*, 2004, **121**, 9776–9792.
62. A. Heyden, A. T. Bell and F. J. Keil, *J. Chem. Phys.*, 2005, **123**, 224101.
63. M. Faheem, S. Suthirakun and A. Heyden, *J. Phys. Chem. C*, 2012, **116**, 22458–22462.
64. R. Ahlrichs, M. Bär, M. Häser, H. Horn and C. Kölmel, *Chemical Physics Letters*, 1989, **162**, 165–169.
65. O. Treutler and R. Ahlrichs, *J. Chem. Phys.*, 1995, **102**, 346–354.
66. C. F. Schwenk and B. M. Rode, *J. Am. Chem. Soc.*, 2004, **126**, 12786–12787.
67. K. Eichkorn, O. Treutler, H. Öhm, M. Häser and R. Ahlrichs, *Chemical Physics*, 1995, **242**, 652–660.
68. K. Eichkorn, F. Weigend, O. Treutler and R. Ahlrichs, *Theor Chem Acta*, 1997, **97**, 119–124.
69. M. V. Arnim and R. Ahlrichs, *Journal of Computational Chemistry*, 1998, **19**, 1746–1757.
70. A. Klamt, *J. Phys. Chem.*, 1995, **99**, 2224–2235.
71. A. Klamt, V. Jonas, T. Bürger and J. C. W. Lohrenz, *J. Phys. Chem. A*, 1998, **102**, 5074–5085.
72. K. N. Marsh, *J. Chem. Eng. Data*, 2006, **51**, 1480–1480.
73. A. Schäfer, H. Horn and R. Ahlrichs, *J. Chem. Phys.*, 1992, **97**, 2571–2577.
74. A. Schäfer, C. Huber and R. Ahlrichs, *J. Chem. Phys.*, 1994, **100**, 5829–5835.
75. F. Weigend, F. Furche and R. Ahlrichs, *J. Chem. Phys.*, 2003, **119**, 12753–12762.
76. A. K. Rappe, C. J. Casewit, K. S. Colwell, W. A. Goddard and W. M. Skiff, *J. Am. Chem. Soc.*, 1992, **114**, 10024–10035.
77. X. Zhang, A. Savara and R. B. Getman, *J. Chem. Theory Comput.*, 2020, **16**, 2680–2691.
78. L. C. Grabow, B. Hvolbæk and J. K. Nørskov, *Top Catal*, 2010, **53**, 298–310.
79. M. Johansson, E. Skulason, G. Nielsen, S. Murphy, R. M. Nielsen and I. Chorkendorff, *SURF SCI*, 2010, **604**, 718–729.